Membrane proteins bind lipids selectively to modulate their structure and function

Arthur Laganowsky[#1,*], **Eamonn Reading**[#1], **Timothy M. Allison**[1], **Martin B. Ulmschneider**[2], **Matteo T. Degiacomi**[1], **Andrew J. Baldwin**[1], and **Carol V. Robinson**[1,*]

[1]Department of Chemistry, University of Oxford, South Parks Road, Oxford, OX1 5QY, UK
[2]Department of Materials Science and Engineering, Johns Hopkins University, Baltimore, Maryland

[#] These authors contributed equally to this work.

Abstract

Previous studies have established that the folding, structure and function of membrane proteins are influenced by their lipid environments[1-7] and that lipids can bind to specific sites, for example in potassium channels[8]. Fundamental questions remain however regarding the extent of membrane protein selectivity toward lipids. Here we report a mass spectrometry (MS) approach designed to determine the selectivity of lipid binding to membrane protein complexes. We investigate the mechanosensitive channel of large conductance (MscL), aquaporin Z (AqpZ), and the ammonia channel (AmtB) using ion mobility MS (IM-MS), which reports gas-phase collision cross sections. We demonstrate that folded conformations of membrane protein complexes can exist in the gas-phase. By resolving lipid-bound states we then rank bound lipids based on their ability to resist gas phase unfolding and thereby stabilize membrane protein structure. Results show that lipids bind non-selectively and with high avidity to MscL, all imparting comparable stability, the highest-ranking lipid however is phosphatidylinositol phosphate, in line with its proposed functional role in mechanosensation[9]. AqpZ is also stabilized by many lipids with cardiolipin imparting the most significant resistance to unfolding. Subsequently, through functional assays, we discover that cardiolipin modulates AqpZ function. Analogous experiments identify AmtB as being highly selective for phosphatidylglycerol prompting us to obtain an X-ray structure in this lipid membrane-like environment. The 2.3Å resolution structure, when compared with others obtained without lipid bound, reveals distinct conformational changes that reposition AmtB residues to interact with the lipid bilayer. Overall our results demonstrate that resistance to unfolding correlates with specific lipid-binding events enabling distinction of lipids that merely bind from

[*]Correspondence and requests for materials should be addressed to A.L. (art.laganowsky@chem.ox.ac.uk) or C.V.R. (carol.robinson@chem.ox.ac.uk).

those that modulate membrane protein structure and/or function. We anticipate that these findings will be influential not only for defining the selectivity of membrane proteins toward lipids but also for understanding the role of lipids in modulating function or drug binding.

Three membrane protein complexes were selected to give a range of topologies, oligomeric states and anticipated selectivity towards lipids: (i) the pentameric MscL from *Mycobacterium tuberculosis* with two transmembrane helices (TMH) per subunit and an intimate relationship with lipids[10,11]; (ii) the tetrameric water efflux channel AqpZ from *Escherichia coli* (*E. coli*) with six TMH for which associated lipid or detergent molecules have been revealed in crystal structures and in related homologues[12,13]; and (iii) the trimeric AmtB from *E. coli*, with eleven TMH involved in the transport of ammonia, for which no lipid binding has been observed to date in crystal structures[14].

Our first objective for studying membrane protein lipid interactions by MS was to maintain the native state of these multimeric assemblies in the gas-phase, devoid of detergent from the micelles required for their introduction[15], such that stabilization by lipid binding could be deduced (Fig. 1a). This had not been possible previously since the conditions needed to disrupt the micelle perturbed the folded state of membrane protein complexes. We screened non-ionic detergents[16] and employed ion mobility MS (IM-MS) (Supplementary Video 1), a technique that measures the rotationally averaged collision cross sections (CCS) of protein complexes in the gas-phase[17]. We found that in detergents commonly used for structural studies (n-dodecyl-β-D-maltoside (DDM), octyl glucose neopentyl glycol (OGNG) and n-nonyl-β-D-glucopyranoside (NG)) the CCS of all charge states were significantly greater when emerged from the micelle than those calculated for the crystal structure, indicative of substantial gas-phase unfolding (Extended Data Figure 1). Interestingly for tetraethylene glycol monooctyl ether (C_8E_4) lower average charge states were observed with CCS in agreement with those calculated for the crystal structures, thus providing optimal conditions for MS of intact membrane protein complexes.

To assess individual lipid binding events we prepared a series of synthetic and natural lipid solutions and added these to protein complexes in C_8E_4 (Extended Data Figure 2). MscL was interrogated first, revealing well-resolved mass spectral peaks corresponding to populations of MscL in complex with one to five lipids (Fig. 1b and Extended Data Figure 3). Unlike other biophysical approaches, which report an average of all species in solution, whether bound or unbound, discrete lipid-bound states can be resolved and interrogated individually, allowing us to obtain CCS for individual lipid-binding events and to assess their effects on stability. Obtaining the native state of these lipid-bound complexes enabled us to explore molecular dynamic simulations combined with filtering using CCS measurements[18] to locate probable lipid-binding sites (Extended Data Figure 4-5 and Supplementary Discussion). We then applied collision-induced unfolding, analogous to that used previously for studying ligand binding to soluble complexes[19]. An increase in CCS, from the trend line calculated for the native state, is observed with increasing collision voltage and is assigned to highly extended conformers (Fig. 1b and Supplementary Video 2). All species, *apo* and one to five phospholipid-bound forms, are measured within the same

experiment enabling a direct comparison, and show less unfolding of native pentameric states as a function of lipid binding.

To extract quantitative values for the effects of lipid binding we applied an equilibrium unfolding model, used extensively in solution studies involving chemical denaturation[20,21]. Plotting CCS against collision voltage reveals unfolding trajectories from the native state, through intermediates, to extended forms. Importantly the oligomeric state is maintained throughout the unfolding experiment (Extended Data Figure 6 and Fig. 1c). We identified four distinct intermediate states in the unfolding trajectories and by comparing the *apo* form with lipid-bound states we calculated the stabilization imparted at the transitions by each lipid (see Methods). The stabilization computed for bound lipids allows us to compare and rank seven different lipids, as well as synthetic phosphatidylcholine (PC) lipids with chain lengths varying from C14 to C22. Despite differences in these lipid structures, we found that all stabilized MscL to a similar degree, consistent with a previous fluorescence study with engineered Trp residues[22] (Fig. 1d and Extended Data Figure 3b-c). We also found that MscL avidly bound phosphatidylinositol phosphate (PI), greater than all other lipids investigated, conferring a large linear increase in stability upon binding multiple PI molecules.

We applied a similar procedure to AqpZ, revealing well-resolved lipid binding and a CCS in agreement with that of the crystal structure of AqpZ (Fig. 2a, and Extended Data Figure 7). Monitoring unfolding trajectories for lipid-bound states of AqpZ showed similar transition points between the different states that were largely independent of the bound lipid. This implies that the lipids investigated had similar effects on resistance to unfolding (Fig. 2b and Supplementary Video 3). As successive lipids are added, from one to three, stabilization is increased *via* regular increments consistent with a linear, cumulative effect. The only exception to this is cardiolipin (CDL), where binding resulted in a substantial increase in protein stability compared to all other lipids. Intrigued by this observation we performed functional assays[23] of the channel reconstituted into liposomes of varying lipid composition. Water permeability assays of AqpZ reconstituted in a total polar lipid extract from a CDL-deficient *E. coli* strain[24] (BKT22) showed a dramatic reduction in water transport compared to the channel reconstituted in wild-type *E. coli* polar lipid preparations (EPL) (Fig. 2c and Extended Data Figure 8). Moreover, reconstituting AqpZ in a lipid preparation from strain BKT22 expressing cardiolipin synthase genes[24], restores CDL to near wild-type levels (mole percentage of 6.6 *versus* 9.1), and results in water transport activity comparable to in EPL (Fig. 2c). These results clearly demonstrate CDL modulates the function of AqpZ.

Analogous IM-MS experiments carried out on AmtB show that resistance to gas-phase unfolding following binding of anionic lipids, phosphatidic acid (PA) and phosphatidylserine (PS), is not correlated with significant stabilization of the channel (Fig. 3). Zwitterionic lipids, PC and phosphatidylethanolamine (PE), confer only moderate stabilization. By contrast, addition of CDL or phosphatidylglycerol (PG) results in dramatic increases in stabilization with cumulative binding of PG increasing protein stability linearly (Fig. 3b, Extended Data Figure 7 and Supplementary Video 4). These results therefore reveal a defined selectivity for PG-like head groups.

To understand the origin of this observed selectivity we crystallized AmtB in the presence of PG. A screen produced X-ray-grade crystals and led to structure determination at 2.3 Å resolution (Extended Data Table 1). The structure of AmtB is composed of three protein subunits, each comprising 11 TMH[14], with two trimers located in the asymmetric unit (Fig. 4). We resolved eight PG molecules in the electron density on the periplasmic side of AmtB (Extended Data Figure 9), a potential ninth PG molecule having ambiguous electron density. Two of the PG molecules are located in similar positions at the subunit interface, with headgroups not in contact with the protein (Fig. 4b). The overall structure is similar to the 20 previously reported in the Protein Data Bank (PDB) determined from detergent-only environments. Major differences arise from a distinct conformational change in a loop, residues 70-81, forming a specific lipid-binding site (Fig. 4c, Supplementary Video 5, and Supplementary Discussion). PG forms hydrogen bonds to N72 and E70 and a water bridge to N79. F75 flips downward to interact with a lipid tail of PG. In addition, several residues are repositioned to interact with the phospholipid bilayer. L81 and I78 shift into the hydrophobic environment of the lipid bilayer. Significantly, W80 moves almost 4 Å (Cα to Cα), its sidechain rotated 160° compared to other structures. This rotation relocates the W80 sidechain from a protein environment into one that is ideally positioned to interact with headgroups of phospholipids, consistent with their alignment along the lipid bilayer interface (Extended Data Figure 9d)[25]. Furthermore, mutation of N72 and N79 to alanine (AmtB[N72A/N79A]), engineered to abolish the specific lipid-binding site, results in the loss of PG induced gas-phase stability (Fig. 3b), consistent with our IM-MS approach identifying specific lipid binding events.

By resolving individual lipid-bound states of membrane protein complexes within the mass spectrometer, and interrogating their stability through gas-phase unfolding, we obtained quantitative values to rank lipid-binding interactions. MscL binds lipids non-selectively, without regard to particular headgroup or chain length, and binding of any lipid imparts comparable stability, in accord with the ability of the channel to bind and respond promiscuously to lipid composition[11,26]. The most significant cumulative effects on stability were observed upon binding of PI, proposed as the functional lipid in the *Mycobacterium* membrane involved in MscL mechanosensitivity[9]. Similarly, AqpZ was found to be non-selective for a number of lipids suggesting comparable binding modes, in line with the two-dimensional crystals of Aqp0[13,27]. The only exception to this non-selective lipid binding is CDL, which significantly stabilizes AqpZ and directly modulates function, as suggested in a previous *in vivo* study[28]. Interestingly, CDL levels in *E. coli* depend on growth conditions, a higher abundance of CDL being present in the stationary phase[24], implying AqpZ function is fine-tuned through modulation of CDL levels. In contrast to the other two systems our finding that AmtB responds only weakly to the majority of lipids is consistent with its extensive transmembrane structure and inherent stability devoid of the lipid bilayer[29]. However, its unexpectedly high selectivity for PG led to the first crystal structure of AmtB in complex with lipid, allowing effects on stability to be rationalized and further validated by mutation of residues forming the specific lipid-binding site.

By investigating a diverse set of membrane proteins and their lipid-binding properties we have extended many seminal studies[1-8] by demonstrating different degrees of selectivity in

lipid binding with AmtB>AqpZ>MscL. Despite these differences in selectivity, in all cases the most stabilizing lipids have a direct influence on the structure and function of the membrane proteins studied, as proposed for PI binding to MscL[9] and demonstrated for CDL and PG binding to AqpZ and AmtB respectively. As membrane proteins are intimately embedded in the bilayer, the relative lipid abundances as well as differences in selectivity can enforce the recruitment of a local lipid environment[30] thus providing an elegant means for fine-tuning membrane protein structure and function.

Methods

Plasmid construction

Two expression plasmids were constructed by subcloning the multiple cloning site region from XbaI (New England Biolabs) and BlpI (New England Biolabs) of pET23b (Novagen) into the backbone pET15b (Novagen). The resulting engineered vector was linearized by NdeI (New England Biolabs) and XhoI (New England Biolabs), gel purified (QIAquick Gel Extraction Kit, Qiagen), and used in subsequent Infusion cloning reactions (Clonetech) to generate a TEV protease cleavable C-terminal fusion to superfolder GFP (subcloned from Gandhi *et al.* 2012[31]) followed by a 6x His-tag or a TEV protease cleavable N-terminal fusion to maltose binding protein (MBP) preceded by a secretion signal peptide (pelB) and 10x His-tag subcloned from Hilf *et al.* 2008[32]. The resulting N- and C-terminal fusion vectors were linearized with NheI and XhoI or NdeI and NheI, gel purified, and used in subsequent Infusion cloning reactions. AmtB (residues 26-428), AqpZ and MscL genes were amplified by polymerase chain reaction (PCR) with Phusion high-fidelity DNA polymerase (New England Biolabs) from prepared *E. coli* BL21 (DE3) genomic DNA (Qiagen) or template plasmid DNA with primers designed for an Infusion cloning reaction using the manufacturer's online tool. The PCR products were purified by agarose gel electrophoresis and extracted using the QIAquick gel extraction kit (Qiagen). The PCR products and linearized vectors (described above) were used in Infusion cloning reactions (Clonetech) to generate MBP-AmtB, AqpZ-GFP and MscL-GFP. MBP-AmtB$^{N72A/N79A}$ was achieved by two-rounds of site-directed mutagenesis using a QuikChange Lightning Multi Site-Directed Mutagenesis Kit (Stratagene, La Jolla, CA) according to the manufacturer's protocol. AqpZ harboring a TEV protease cleavable N-terminal 6x His-tag (NHis-AqpZ) was constructed through an infusion cloning reaction of AqpZ and a custom pRSFDuet-1 vector (Novagen), N-terminal coding sequence between NcoI and BamHI was replaced with the following nucleotide sequence ccatggggcagcagccatcaccatcatcaccacgagaacctgtacttccagggtggatcc, linearized with BamHI and XhoI. All constructs were verified by DNA sequencing.

Generation of E. coli BL21(DE3) mscL::Kan^R strain

Homologous recombination mediated chromosomal disruption of *mscL* was performed using the Gene Doctoring method[33]. Briefly, 900 base pairs flanking the 5′ and 3′ ends of the *mscL* gene were subcloned into the pDOC-K plasmid resulting in these regions flanking a kanamycin resistance (Kan^R) cassette. This plasmid and the recombineering plasmid, pACBSCE, were transformed into *E. coli* BL21 (DE3) Gold (Agilent). Homologous recombination was carried out by induction of λ–Red recombinase system and SceI endonuclease with arabinose. Recombinants harboring gene disruption with Kan^R were

selected on kanamycin and sucrose, and verified by colony PCR. Calcium chloride competent cells were made as described by Drew *et al.*[34].

Membrane protein expression

MBP-AmtB and AqpZ-GFP plasmids were transformed into *E. coli* BL21 (DE3) Gold (Agilent). MBPAmtB[N72A/N79A] and NHis-AqpZ were transformed into *E. coli* OverExpress™ C43 (DE3) (Lucigen). MscL-GFP was transformed into *E. coli* BL21(DE3) *mscL::KanR* (described above). Several colonies were inoculated into 50 mL LB Miller (5 g yeast extract, 10 g peptone from casein, and 10 g sodium chloride per liter) and grown overnight at 37 °C. One liter of LB in 2 L shaker flasks was inoculated with 7 mL of overnight culture and grown at 37 °C until the culture reached an OD_{600} between 0.6-0.8. Isopropyl β-D-1-thiogalactopyranoside (IPTG) was added to the culture at a final concentration of 0.5 mM and grown for 3 hours at 37 °C. Cells were harvested by centrifugation at 5,000 g for 10 minutes at 4 °C. Cell pellets were resuspended in phosphate-buffered saline, pelleted by centrifugation at 5,000 g for 10 minutes at 4 °C and stored at −80 °C.

Purification of membranes

Membranes were purified as described by Newby *et al.*[35] with minor modifications. Cell pellets were thawed and resuspended at 20 mL per liter of culture in Buffer A (300 mM sodium chloride, and 20 mM 2-amino-2-hydroxymethyl-propane-1,3-diol (Tris), pH 7.4 at room temperature) supplemented with a complete protease inhibitor tablet (Roche) and 5 mM beta-mercaptoethanol (BME). Cell suspension was passed several times through an M-110 PS microfluidizer (Microfluidics) at 19,000 psi. Insoluble material was pelleted by centrifugation at 20,000 g for 25 minutes at 4 °C. Membranes were pelleted by centrifugation at 100,000 g for 2 hours at 4 °C. Membranes were resuspended in ice-cold Buffer B (100 mM sodium chloride, 20% glycerol, 5 mM BME, and 20 mM Tris, pH 7.4 at room temperature), homogenized using a Potter-Elvehjem Teflon pestle and glass tube. For MscLGFP, glycerol was omitted from Buffer B. Resuspended membranes were used either directly or flash frozen in liquid nitrogen and stored at −80 °C.

AmtB-GFP detergent screen

A membrane protein detergent screen on AmtB-GFP was performed as previously described[16] with minor modifications. Briefly, AmtB-GFP was extracted from purified membranes (described above) with 1-2% (w/v) of the detergent of interest in Buffer B and incubated for one to three hours at room temperature or overnight at 4 °C with gentle agitation. Insoluble material was pelleted by centrifugation at 20,000 g for 25 minutes at 4 °C. The clarified supernatant was loaded onto small Ni-NTA agarose (Qiagen) drip columns (Bio-spin Chromatography columns, Bio-Rad) and washed with several column volumes of Buffer C (200 mM sodium chloride, 20 mM imidazole, 5 mM BME, 50 mM Tris, pH 8.0 at room temperature) supplemented with two times the critical micelle concentration (CMC) of the detergent of interest. AmtB-GFP was eluted with two column volumes of Buffer D (100 mM sodium chloride, 250 mM imidazole, 5 mM BME, 2x CMC detergent of interest, and 50 mM Tris, pH 8.0 at room temperature). Eluted protein was concentrated using a 100 kDa

Molecular Weight Cutoff (MWCO) concentrator and buffer exchanged into MS Buffer (2x CMC detergent of interest and 200 mM ammonium acetate, pH 8.0 with ammonium hydroxide) using a centrifugal buffer exchange device (Micro Bio-Spin 6, Bio-Rad).

Purification of membrane proteins

MBP-AmtB, MBP-AmtB[N72A/N79A] and AqpZ-GFP were extracted from purified membranes in Buffer B supplemented with 200 mM OG and incubated with gentle agitation overnight at 4 °C. MscL was extracted from purified membranes with glycerol-free Buffer B supplemented with 1% OGNG. Extracted membrane proteins were clarified by centrifugation at 20,000 g for 25 minutes at 4 °C. Supernatant was filtered before loading onto a 5 mL HisTrap-HP column (GE Healthcare, Piscataway, NJ) equilibrated in Buffer E (200 mM sodium chloride, 10% glycerol, 20 mM imidazole, 0.025% DDM, and 50 mM Tris, pH 7.4 at room temperature). After the clarified supernatant was loaded, the column was initially washed with 40-50 mL of DDM-free Buffer E supplemented with 1% OG for MBP-AmtB and AqpZ-GFP, and 0.5% OGNG for MscL-GFP. Membrane proteins were then exchanged into several column volumes of Buffer E until a steady baseline was reached. Membrane protein fusions were eluted with a linear gradient to 100% in two column volumes of Buffer F (100 mM sodium chloride, 10% glycerol, 500 mM imidazole, 0.025% DDM, and 50 mM Tris, pH 7.4 at room temperature). Peak fractions were pooled, supplemented with 5 mM BME and His-tagged TEV protease[36,37], and dialyzed against Buffer G (150 mM sodium chloride, 10% glycerol, 20 mM imidazole, 0.025% DDM, and 50 mM Tris, pH 7.4 at room temperature) overnight at 4 °C. After overnight incubation, samples were filtered and passed back over a 5 mL HisTrap-HP column equilibrated in Buffer E. Flow through containing the untagged membrane protein was collected and concentrated using a 100 kDa MWCO concentrator. Notably, tag-removed membrane proteins with fusions to the C-terminus contained additional protein sequence ASGENLYFQ, or GAS for N-terminally tagged proteins, resulting from the TEV protease recognition sequence and cloning restriction site. Concentrated protein was either used immediately or flash-frozen in liquid nitrogen and stored at −80 °C. Protein concentration was measured using Biomate UV detector with the following calculated extinction coefficients[38] of 1.57, 1.484, and 0.265 g/L•cm$^{−1}$ for AmtB, AqpZ, and MscL, respectively.

NHis-AqpZ was purified as previously described[39]. Briefly, extracted and clarified membrane proteins were loaded onto a 5 mL HisTrap-HP column (GE Healthcare, Piscataway, NJ) equilibrated in buffer (200 mM sodium chloride, 10% glycerol, 20 mM imidazole, 1% OG, and 50 mM Tris, pH 7.4 at room temperature). NHis-AqpZ was eluted with a linear gradient to 100% elution buffer (100 mM sodium chloride, 10% glycerol, 500 mM imidazole, 1% OG, and 50 mM Tris, pH 7.4 at room temperature) over two column volumes. Peak fractions containing NHis-AqpZ were concentrated prior to imidazole removal using two 5 mL HiTrap Desalting columns (GE Healthcare, Piscataway, NJ) in tandem. Peak fractions were pooled and NHis-AqpZ was concentrated using a 50 kDa MWCO concentrator.

Preparation of membrane proteins for native mass spectrometry

Either flash frozen samples thawed on ice or fresh samples were detergent exchanged by gel filtration chromatography. Membrane protein samples were injected onto a Superdex 200 GL 10/300 (GE Healthcare) column equilibrated in Buffer H (130 mM sodium chloride, 10% glycerol, and 50 mM Tris, pH 7.4 at room temperature) supplemented with either 0.5% of C_8E_4, 0.4% of NG, 0.116% OGNG, or 0.025% of DDM. Peak fractions containing the detergent-exchanged membrane protein complex were concentrated. A 50 kDa MWCO concentrator was used to concentrate samples in the detergent C_8E_4 and 100 kDa MWCO concentrator used on membrane protein complexes in all other detergents. Concentrated proteins were either used directly or flash-frozen in liquid nitrogen and stored at −80 °C. Notably, we found no observable difference in mass spectra quality after a single freeze-thaw of membrane proteins throughout our purification regime. Purified membrane proteins were buffer exchanged into MS Buffer (two times the CMC of detergent of interest and 200 mM ammonium acetate, pH 7.2-8.0 with ammonium hydroxide) using a centrifugal buffer exchange device (Micro Bio-Spin 6, Bio-Rad) as previously described[16]. Membrane proteins detergent exchanged into MS Buffer supplemented with C_8E_4 or OGNG could be flash frozen without compromising mass spectra quality unlike MS Buffer supplemented with NG or DDM.

Preparation and titration of phospholipids

Phospholipids were purchased from Avanti (Avanti Polar Lipids Inc., Alabama, USA) and prepared at stock concentrations of 10 mg/ml in 200 mM ammonium acetate pH 8.0 as previously described[16]. The membrane protein complex to phospholipid to detergent ratio (P:L:D) was optimized for each membrane protein complex to achieve consistency of nanoelectrospray and resolved mass spectral peaks of bound phospholipid throughout the gas-phase unfolding series (Extended Data Figure 2b). Phospholipid preparations were added to buffer exchanged membrane protein complexes followed by equilibration at room temperature for 10-30 minutes before MS analysis. Notably by MS we did not observe a significant increase in bound phospholipid with longer incubation times.

Mass spectrometry

Mass spectrometer settings were initially set to values for membrane proteins as previously described[16] for a modified Q-TOF 2 mass spectrometer (Micromass, Manchester, UK) with a Z-spray source[40]. Typical instrument values were 5-7 μbar for source pressure, 1.5-1.8 kV for capillary voltage, 150-190 V for cone voltage, 1-10 V for extraction voltage, 180-200 V for collision voltage, argon for collisional gas, and 0.2-0.3 MPa argon gas pressure.

Ion mobility mass spectrometry

Ion mobility measurements were performed on a Synapt G2 (where noted) or on a modified Synapt G1 HDMS instrument with the travelling-wave ion mobility cell replaced by an 18-cm drift cell with radial RF ion confinement and a linear voltage gradient to direct ions along the axis of transmission to the time-of-flight (TOF) mass analyzer[41]. The ion mobility mass spectrometer was typically set to a source pressure of 5-7 mBar, capillary voltage of 1.4-1.7 kV, capillary nanoflow of 0.03-0.2 mBar and argon as collision gas with flow rate

set to 5-8 mL/min (~6.6-6.7 e^{-2} mBar). Collision voltage ranged from 50-240 V with measurements taken at 5 V and 2 V steps for monitoring gas-phase unfolding of membrane protein complexes. The sample and extraction cone, and trap bias voltages, quadrupole profile, and collision (trap) gas pressure were optimized for maximal ion intensity of the target membrane protein complex. Helium was the drift cell gas and was set to a pressure of ~1.6-1.8 Torr (40 ml/min flow rate). Pusher time, pulse width and TDC inhibit were set to 180, 7 and 7 µs, respectively. The ion guide/source (300 ms^{-1}, 10 V), trap (300 ms^{-1}, 0.2 V) and transfer (100 ms^{-1}, 10 V) travelling wave velocities and wave heights were kept constant. The mobility release time was set at 200 µs with a trap voltage of 30 V and extract voltage of 10 V. Pressure and temperature of the ion mobility cell was measured directly.

Ion drift time (t_d) was determined as previously described[41]. Briefly, t_d was determined by subtracting the non-drift time component (t_o) from the ion arrival time (t_a)

$$t_d = t_a - t_o$$

t_o was determined by extrapolation from linear plots of t_a versus V^{-1} over ten different voltage potentials (Extended Data Figure 1d). Ion drift time was converted to a rotationally averaged ion-neutral collision cross section (CCS) (Ω) using the Mason-Schamp equation[42]

$$\Omega = \frac{(18\pi)^{\frac{1}{2}}}{16} \frac{ze}{(k_b T)^{\frac{1}{2}}} \frac{1}{N} \frac{t_d V}{L^2} \frac{p_0}{p} \frac{T}{T_0} \sqrt{\frac{1}{\mu}}$$

where z is the charge on the ion, μ the reduced mass of the ion-neutral in the drift chamber, N is the drift gas number density, k_b is the Boltzmann constant, e is the charge on the electron, V is the potential voltage across the drift cell, p is the pressure of the drift cell, T is the thermodynamic temperature of the drift cell, L is the length of the drift tube, T_o is standard temperature, and p_o is standard pressure.

Travelling wave ion mobility measurements (TW-IMS) were performed on a commercially available Synapt G2 (Waters). Source pressure set to 5-7 mBar, capillary voltage of 1.4-1.7 kV, capillary nanoflow of 0.03-0.2 mBar and argon as collision (trap) gas at flow rate of 8.0 ml/min. Collision voltage ranged from 50-200 V with measurements taken at 5 V step intervals for monitoring gas-phase unfolding of membrane complexes. The sample and extraction cone and trap bias voltages, quadrupole profile, and collision gas pressure were optimized for maximal ion intensity of the target membrane protein complex. Helium was the IMS entrance cell gas set to a flow rate of 180 ml/min and the drift cell gas was nitrogen set to flow rate of 90 ml/min. The EDC delay coefficient was 1.57 µs. The trap wave velocity and wave height were 300 ms^{-1} and 8.0 V, respectively. The IMS wave velocity and wave height were 300 ms^{-1} and 30.0 V, respectively. The transfer wave velocity and wave height were 100 ms^{-1} and 2.0 V, respectively. The mobility release time was set at 200 µs with a trap voltage of 30 V and extract voltage of 10 V. Gas-phase unfolding profiles are largely similar to those collected on a drift cell instrument (Extended Data Figure 6d).

Collision cross section calculations

The Projection Approximation (PA) calculation within a modified version of MOBCAL[18,43,44] used to calculate the Ω_{PA} from respective crystal structure coordinates. CCS values were corrected $\Omega_{Corr'}$ by the correction factor of 1.14 and missing residues between the protein construct (M_{Exp}) and crystal structure (M_{PDB})[45,46]

$$\Omega_{Corr'} = 1.14 \Omega_{PA} \left(\frac{M_{Exp}}{m_{PDB}} \right)^{\frac{2}{3}}$$

This correction has been shown to give values that correlate with known values to ±3%[41,47].

Gas-phase unfolding data analysis and modeling

Mass spectra and ion mobility data were analyzed using in-house software written in the Python programming language with a graphical user interface constructed using wxPython (manuscript in preparation). Briefly, MS-only data collected on a Q-TOF 2 instrument was smoothed with MassLynx software prior to being imported and linearized at a step size of one in m/z. Theoretical mass spectra were predicted following equations described in Stengel *et al.*[48]. Mass, average charge state, width of charge state distribution, resolution, and concentration were fitted to experimental data with least squares regression of the pseudo-χ^2 function[48].
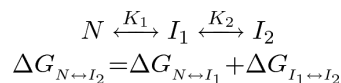
Ion mobility data were imported using a custom script provided by Waters at an *m/z* resolution of four in drift data and one in mass spectra for fitting. Mass spectra were smoothed and theoretical mass spectra were fitted as described above. A standardized integration window was employed for extracting arrival time distributions (ATD) using a resolution (R = $m/z \div m/z$) of 1000 and a height cut-off of 25% for the modeled Gaussian to the respective *m/z* peak. To generate gas-phase unfolding plots, ATDs were extracted for the given *m/z* peak using the standardized integration window followed by normalization. To convert to a CCS axis, arrival time was directly converted to CCS using equations above. This procedure generates gas-phase unfolding data and are plotted using Matplotlib[49]. All ion mobility mass spectra are shown in linear scale.

To a first order approximation, gas-phase unfolding of protein complexes, like unfolding in solution, will be linearly dependent (*m*) on collision voltage (*CV*)

$$\Delta G = \Delta G^0 - m[CV]$$

where ΔG is free energy of unfolding and ΔG^0 is the free energy of the system at zero collision voltage in the gas-phase. Using this assumption, two, three, four, and five state linear equilibrium unfolding models were used to model the abundance of native and non-native species. Notably, two new free parameters are introduced for each new species. Two, three, four and five state unfolding models were fitted to the data, and an F-test was used to decide if the fitting quality is sufficiently improved as to justify the inclusion of additional fitting parameters. The most abundance charge state of the three membrane protein

complexes agreed with a four state unfolding model. For example, in the case of three unfolding species we used the following thermodynamic denaturing unfolding model[20].

$$N \xleftrightarrow{K_1} I_1 \xleftrightarrow{K_2} I_2$$
$$\Delta G_{N \leftrightarrow I_2} = \Delta G_{N \leftrightarrow I_1} + \Delta G_{I_1 \leftrightarrow I_2}$$

Expansion of $G_{N \leftrightarrow I_1}$ gives the following,

$$\Delta G_{N \leftrightarrow I_1} = \Delta G^0_{N \leftrightarrow I_1} - m_{N \leftrightarrow I_1}[CV]$$
$$\Delta G_{N \leftrightarrow I_1} = -RTlnK_1$$
$$K_1 = \frac{F_{I_1}}{F_N}$$

where F is a mole fraction. The sum of mole fractions of native (F_N), and non-native species (F_{I_1} and F_{I_2}) is equal to 1.

$$F_N + F_{I_1} + F_{I_2} = 1$$

We can generalize this taking into account the entire relationships one can obtain the fraction of native and non-native given K_1 and K_2

$$
\begin{aligned}
F_N &= \frac{1}{1 + K_1 + (K_1 \cdot K_2)} \\
F_{I_1} &= \frac{K_1}{1 + K_1 + (K_1 \cdot K_2)} \\
F_{I_2} &= \frac{K_1 \cdot K_2}{1 + K_1 + (K_1 \cdot K_2)}
\end{aligned}
$$

The respective $G°$ and m parameters were solved numerically. In the two species case one can obtain a closed form solution, however, it is both efficient and general to solve numerically.

An irreversible kinetic unfolding model as an alternative for modeling gas-phase unfolding data was also explored. The irreversible unfolding model defines the degree of unfolding as being related to time. By changing the potential across the drift cell, the time ions spend in the ion mobility drift cell post collision-induced unfolding can be altered over several orders of magnitude. The relative abundances of unfolded intermediates species as a function of drift time was monitored for a membrane protein complex. There was no significant change in relative abundances over a four-fold increase in time (Extended Data Figure 6e-f) demonstrating that the unfolding mechanism does not agree with an irreversible kinetic model for the unfolding model and no further unfolding occurs post collision cell. Data are in excellent agreement however with a reversible model as described above.

Ion mobility intensities were extracted for native and unfolded CCS species at various collision voltages. With the assumption that signal intensity is approximately proportional to species concentration, the data can be converted to a molar fraction to generate two dimensional (2D) data, which can be fitted to an equilibrium unfolding model. Minimized

2D parameters were used as a seed for three dimensional (3D) fitting of gas-phase unfolding data.

From the unfolding curve, and parameters m, $G°$, CCS_μ (mean of CCS species), CCS_σ (standard deviation of CCS species), the 3D data can be fit. First, a CCS range was selected for each native and unfolded species in the unfolding plot. These CCS ranges provided the initial parameters used to model various CCS species identified by inspection. Next, to make the calculations more efficient the gas-phase unfolding data were trimmed to a minimum and maximum value derived by either subtraction or addition of 10% times the native and last unfolding CCS species, respectively. Trimming resulted in gas-phase unfolding containing on average around 900 data points. The equilibrium unfolding model described above was seeded with the parameters from the minimized 2D data and the molar fraction of species was normalized to match the normalization of experimental data. The fitting surface was rugged and required a sophisticated minimization procedure to maximize the chance of finding global minimum. First the 3D model was minimized using quasi-Newton method of Broyden, Fletcher, Goldfarb, and Shanno (BFGS) available in Scipy[50]. This provided the boundaries for bio-inspired algorithms; all parameters were set to boundaries of ±25% with the exception of the CCS species peak centers which were set to ±5%. The 3D model was minimized using the modified differential algorithm (de_1220) available in PyGMO[51,52] using the following parameters: population of 20; 12 evolutions; 250 generations; and 8 islands. Other algorithms, such as particle swarm and bee colony were screened however the modified differential algorithm produced similar or higher R^2 values in considerably less computation time.

The resulting minimized 3D model enabled quantification of unfolding transitions and stabilization. An unfolding transition occurs when a species with a determined CCS transitions to another CCS species, for example see Extended Data Figure 6c. The transition midpoint, CV_{50} is determined by

$$CV_i = \frac{\Delta G^0}{m}$$

Where CV_i is the value at which 50% of a specific transition state i is depleted. This metric was found to be particularly useful for this application as it removes correlations between $G°$ and m inherent in the fitting procedure. The stabilization of a protein due to the presence of additional phospholipids was quantified according to:

$$\Delta CV_i = CV_i^{lipid} - CV_i^{apo}$$

This comparative approach takes into account to first order any variability in transition collision voltages between repeated measurements for a given protein.

To compare between various proteins and different unfolding states, as well as to average out any systematic and/or inherent variability in droplet formation, the average stabilization was calculated for the bound ligand by,

$$Stabilization = \frac{z\sum_i^T \Delta CV_i}{\zeta}$$

where ζ is the number of transitions, i is a specific transition, and z is the charge state. Averages and standard error of the means was calculated for three repeated measurements. Statistical significance between means were determined by a one-way ANOVA test (N=3) followed by *post-hoc* Tukey analysis. A Shapiro-Wilk test (at the 0.05 level) was used to infer the data was drawn from a normally distributed population. A Brown-Forsythe test (at the 0.05 level) was performed to infer homogeneity of variance prior to means comparison. All statistical tests were performed using OriginPro 8.5.1.

Molecular dynamics preparation and simulation

Crystal structures for the Ammonia Channel AmtB (1U7G)[14], Aquaporin Z (1RC2)[12] and MscL (2OAR)[10] were obtained from the Protein Data Bank and prepared. Molecular simulations were performed using GROMACS 4.5 (www.gromacs.org)[53], with the OPLS all-atom protein force field[54], OPLS united-atom lipid parameters for palmitoyloleoyl-phosphocholine (POPC)[55] and the TIP3P water model[56]. Initial configurations were created using hippo beta (www.biowerkzeug.com).

Electrostatic interactions were computed using the particle mesh Ewald (PME) method[57], and a cutoff of 10 Å was used for van der Waals interactions. Bonds involving hydrogen atoms were restrained using LINCS[58]. Simulations were run with a 2 fs integration time step and neighbor lists were updated every five steps. All simulations are performed in an NPT ensemble, without additional applied surface tension. Solvent (water, ions), lipids, and the protein were each coupled separately to a heat bath at a temperature of 30 °C with time constant $\tau_T = 0.1$ ps using weak temperature coupling[59]. Atmospheric pressure of 1 bar was maintained using weak semi-isotropic pressure coupling with compressibility $\kappa_z = \kappa_{xy} = 4.6\cdot10^{-5}$ bar^{-1} and time constant $\tau_P = 1$ ps[60]. A complete list of simulations is given in Extended Data Figure 4b.

Each protein phospholipid pair generated by MD was treated as a candidate model. For example, ~105,000 such models were generated for AqpZ and filtered by comparison of calculated and experimental CCS values. More specifically, within each MD snapshot there are ~80 lipids that could be in accord with the CCS measurements for one lipid bound to AqpZ. After filtering by agreement with CCS, an ensemble of protein phospholipid complexes consistent with our data was identified. As the MD is used to provide a source of potential lipid associated structures, the results are largely invariant to the choice of force field and lipid molecule.

Identifying lipid binding sites from MD simulations and CCS measurements

The object is to determine which MD frames are in best agreement with the experimental CCS data. For every simulated system, one frame was extracted every 0.2 ns generating 1,000 pdb files for a 500 ns simulation time. For each extracted frame, all lipids within 6 Å of the protein were identified. All possible combinations of these two lipids and protein were

selected. For example for AqpZ and one lipid typically yielded 80 extracted combinations per frame (Extended Data Figure 4c). The CCS value of each combination per frame (f) was calculated using a modified version of MOBCAL[18,43,44]. A ratio ($R_{f,calc}$) was determined using the calculated CCS values for each of the +1 lipid and the +2 lipid-bound states

$$R_{f,l,calc} = \frac{CCS_{protein+lipid,f,l}}{CCS_{ptotein,f}}$$

where $CCS_{protein+lipid}$ is CCS of protein plus number of lipid(s) (l) and $CCS_{protein}$ is CCS of protein. Using a ratio avoided any potential issues associated with taking the difference of uncorrected CCS values determined experimentally. These measurements enable the calculation of three chi-squared (χ^2) values for a given combination of two lipids and protein

$$\chi^2_{f,l} = \frac{(R_{f,l,calc} - R_{f,l,exp})^2}{\sigma^2_l}$$

where $R_{f,exp}$ and σ are the average and standard deviation of the experimental CCS ratio for data with one or two lipid molecules bound from three repeated measurements, and $R_{f,exp}$ is the CCS ratio derived from theoretical calculations. The overall chi-squared values were calculated from:

$$\chi^2_f = \chi^2_{f,2} + \chi^2_{f,1a} + \chi^2_{f,1b}$$

where χ^2_{2f} is the chi-squared calculated for two lipids bound, and $\chi^2_{f,1a}$ and $\chi^2_{f,1b}$ are the chi-squared values for each individual lipid molecule with the protein. In the case where only the +1 lipid CCS data is analyzed, neglecting the +2 lipid data, only one χ^2 value contributed towards the sum. The probability (P_f) that a given protein phospholipid pair with protein matches the data is given by the following Bayesian probability:

$$P_f = e^{\frac{-\left(\chi^2 - \chi^2_{min}\right)}{2}}$$

where χ^2_{min} is the minimum chi-squared value obtained across the entire simulation, whose corresponding P_f is equal to 1, representing the most probable structure. It follows that all candidate lipid pair and protein combinations with a P_f value greater than 0.785 will be one half standard deviation from the most probable structure. The ensemble of structures identified with $P_f >= 0.785$ can be considered the most probable arrangement of lipids and protein found to be consistent with the experimental data. This ensemble of structures was projected onto the surface of the protein to identify the most probable locations of contact between the protein and the lipid.

Total Polar Lipid Extracts from cardiolipin deficient E.coli strain, BKT22

The cardiolipin deficient *E. coli* strain[24], BKT22 (*clsA, clsB, clsC, ymdB::Kan^R*) and calcium chloride competent BKT22 cells were transformed with pBAD-YC (plasmid containing clsC and ymdB genes[24]), referred herein as BKT22-YC, and grown overnight in LB media. Overnight cultures were diluted to an OD_{600} of 0.03 in LB media with the exception that arabinose was added to a final concentration of 0.2% for BKT22-YC to induce expression of cardiolipin genes, clsC and ymdB. The strains were grown for six hours to stationary phase (OD_{600} ~2.0). Cells were harvested by centrifugation at 3,500 *g* at 4°C for 10 min. Cell pellets were resuspended in phosphate-buffered saline followed by centrifugation.

Lipids were extracted using the Folch method[61]. Briefly, cells were resuspended in 20mL of 2:1 (v/v) chloroform:methanol per gram of cells and agitated on a stir plate for 20 min. The mixture was then clarified using filter paper and washed with 0.2 volume of water. The extract was briefly vortexed before centrifugation at $800 \times g$ to separate phases. The upper aqueous phase was removed and the interface was washed with 1:1 (v/v) methanol:water without disturbing the lower organic phase. The lower organic phase was recovered and evaporated under a stream of nitrogen. The dried total lipid extract was then resuspended in diethyl ether to extract polar lipids and evaporated under nitrogen then under vacuum overnight.

Thin Layer Chromatography

HPTLC Silica gel 60 aluminum plates (Merck Millipore) were pre-developed with 1:1 (v/v) chloroform:methanol and left to air-dry overnight. The plates were then impregnated with an adsorbent modifier (1:1 (v/v) 1.2% boric acid in absolute ethanol-water) followed by activation at 100°C for one hour[62]. Samples were spotted and plates developed in 65:25:5 (v/v) chloroform:methanol:acetic acid. After air-drying for 30 min, plates were sprayed with 10% sulphuric acid in ethanol and charred at 200 °C[63]. Molar percent (mol %) of lipid species was determined from the intensity of lipid species using ImageJ 1.47v software[64].

Proteoliposome/liposome preparation

E. coli total polar lipid extract (acetone/ether preparation; Avanti Polar Lipids) was dissolved at 20 mg/ml in 2:1 (v/v) chloroform:methanol to obtain a clear solution. Solvent was evaporated under a stream of nitrogen gas then under vacuum overnight. *E. coli* total polar lipid (EPL), BKT22 and BKT22-YC extracts were hydrated in 2 mM BME to a final concentration of 50 mg/ml and left to incubate for 1 hr at room temperature with constant agitation. These were then split into aliquots and frozen. Lipids were always handled under a nitrogen atmosphere.

Liposomes and proteoliposomes were prepared following previously established protocols[23,39]. Briefly, lipid stocks were diluted into borosilicate tubes to a final concentration of 45 mg/ml in 100 mM MOPS–Na pH 7.5 and pulsed in a bath sonicator until a clear suspension was obtained. A reconstitution mixture (400 μl) was prepared in a borosilicate tube at room temperature by sequentially adding 100 mM Mops–Na (pH 7.5), 1.25 % (wt/vol) OG, purified NHis-AqpZ for proteoliposomes (final concentration 100 μg/

ml), and 10 mg/ml sonicated lipids. After incubation for 1 h at room temperature the mixture was diluted 25 fold into 20 mM HEPES pH 7.5. The liposomes were harvested by centrifugation 140,000 *g* for one hour and resuspended to a final volume of 1.5 ml in 20 mM HEPES pH 7.5. Liposomes and proteoliposomes were stored on ice prior to measurement. EPL, BKT22 and BKT22-YC liposomes/proteoliposomes had an average diameter of 140, 149, and 160 nm determined from dynamic light scattering (Viscotek 802).

AqpZ water permeability assay

Liposome shrinkage was induced by rapidly mixing 1:1 (v/v) proteoliposomes/liposomes with osmolyte buffer (20 mM HEPES pH 7.5, 570 mM sucrose; a 285 milliosmolarity gradient) using a stopped-flow apparatus (Applied Photophysics SX20). Water transport/ permeability was monitored by measuring the light scattering ($\lambda = 600$ nm) of the preparation upon mixing at 8 °C. An increase in signal reflects liposome shrinkage. Light scattering (*L*) data from repeated measurements (*N=5*) were fit to a single exponential rise equation to obtain the rate of water transport (k_{wat}) using OriginPro 8.5.1.

$$L(t) = Ae^{-tk_{wat}} + L_o$$

where *t* is time in msec, *A* is a constant, k_{wat} is rate of water transport, and L_o is the maximum light scattering (typically one for normalized data).
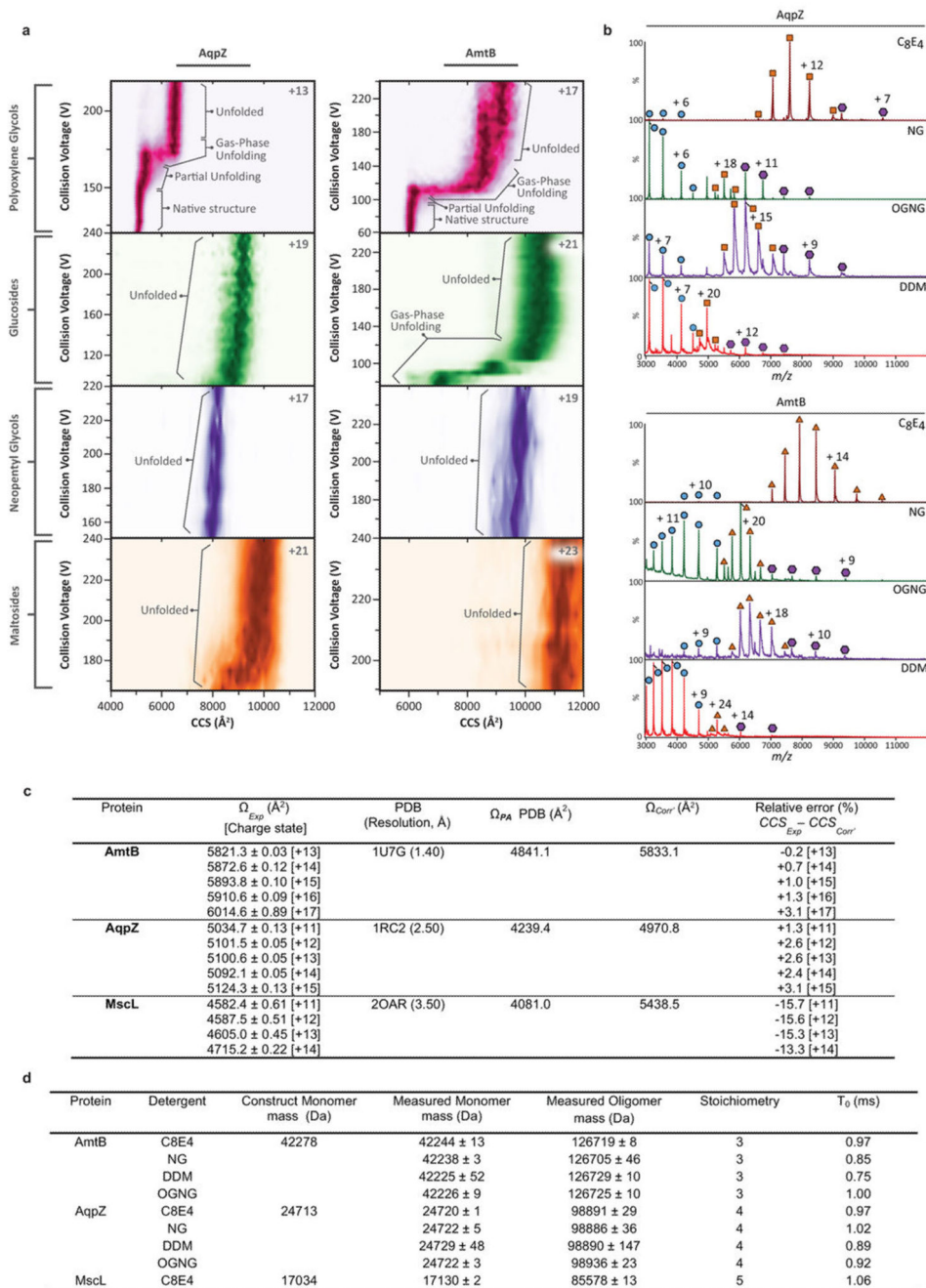
AmtB crystallization and structure determination

AmtB was purified as described for native mass spectrometry experiments with one minor modification. AmtB was detergent exchanged into Buffer H containing 0.5% C_8E_4 using a Superdex 200 10/300 gel filtration column (GE Healthcare). Peak fractions of AmtB from gel filtration were pooled and concentrated to ~15 mg/mL using a 50 kDa MWCO concentrator (Millipore). A ten-fold molar excess of phosphotidylglycerol was added to AmtB prior to crystallization. Crystals of AmtB were grown at 20 °C in hanging drop plates with crystallization solution 15% PEG 4000, 0.8M potassium formate, and 0.1 M sodium acetate pH 4.6. Hexagonal plate crystals appeared after one month.

Single crystals were mounted with CrystalCap HT Cryoloops (Hampton Research, Aliso Viejo, CA) before flash frozen. Data were collected at Diamond Light Source beam line I04. Diffraction data collected at a wavelength of 0.97949Å were processed with XDS[65] in apparent space group P622. Cell content analysis suggested two molecules in the asymmetric cell and attempts to obtain phases from molecular replacement using PHASER[66] with pdb 1U7G resulted in placement of only one molecule with a missing layer of protein molecules. Twinning was suspected and the data were processed into lower symmetry space groups until molecular replacement could correctly place all protein molecules in the asymmetric cell, which turned out to be space group $C222_1$. Data were submitted to the UCLA twin detection server[67] for twinning analysis that indicated partial twinning with $<|L|> = 0.463$ (untwinned=0.5, perfectly twinned =0.375) and $<L2> = 0.291$ (untwinned=0.333, perfectly twinned =0.200). Despite the presence of twinning, initial phases were found by molecular replacement using PHASER with pdb 1U7G placing six molecules in the asymmetric unit cell, and followed automated model building using

PHENIX[68] and manual model building using COOT[69]. All model refinement was done with REFMAC[70] in twin mode. Omit maps were generated first by deleting coordinates of the ligand prior to refinement. Refinement with twinning applied resulted in a 10% drop in both R_{work} and R_{free}, consistent with twinning. Ramachandran plot of the refined structure gave 96% in favoured regions and 0.4% outliers. Figures were generated with PyMOL[71].

Extended Data

c

Protein	Ω_{Exp} (Å^2) [Charge state]	PDB (Resolution, Å)	Ω_{PA} PDB (Å^2)	$\Omega_{Corr'}$ (Å^2)	Relative error (%) $CCS_{Exp} - CCS_{Corr'}$
AmtB	5821.3 ± 0.03 [+13]	1U7G (1.40)	4841.1	5833.1	-0.2 [+13]
	5872.6 ± 0.12 [+14]				+0.7 [+14]
	5893.8 ± 0.10 [+15]				+1.0 [+15]
	5910.6 ± 0.09 [+16]				+1.3 [+16]
	6014.6 ± 0.89 [+17]				+3.1 [+17]
AqpZ	5034.7 ± 0.13 [+11]	1RC2 (2.50)	4239.4	4970.8	+1.3 [+11]
	5101.5 ± 0.05 [+12]				+2.6 [+12]
	5100.6 ± 0.05 [+13]				+2.6 [+13]
	5092.1 ± 0.05 [+14]				+2.4 [+14]
	5124.3 ± 0.13 [+15]				+3.1 [+15]
MscL	4582.4 ± 0.61 [+11]	2OAR (3.50)	4081.0	5438.5	-15.7 [+11]
	4587.5 ± 0.51 [+12]				-15.6 [+12]
	4605.0 ± 0.45 [+13]				-15.3 [+13]
	4715.2 ± 0.22 [+14]				-13.3 [+14]

d

Protein	Detergent	Construct Monomer mass (Da)	Measured Monomer mass (Da)	Measured Oligomer mass (Da)	Stoichiometry	T_0 (ms)
AmtB	C8E4	42278	42244 ± 13	126719 ± 8	3	0.97
	NG		42238 ± 3	126705 ± 46	3	0.85
	DDM		42225 ± 52	126729 ± 10	3	0.75
	OGNG		42226 ± 9	126725 ± 10	3	1.00
AqpZ	C8E4	24713	24720 ± 1	98891 ± 29	4	0.97
	NG		24722 ± 5	98886 ± 36	4	1.02
	DDM		24729 ± 48	98890 ± 147	4	0.89
	OGNG		24722 ± 3	98936 ± 23	4	0.92
MscL	C8E4	17034	17130 ± 2	85578 ± 13	5	1.06

Extended Data Figure 1. Maintaining intact native membrane protein complexes in the mass spectrometer

a-b, Gas-phase unfolding plots (left, 5 V steps) and mass spectra (right) of detergent stripped AqpZ and AmtB ions (charge inset) from different non-ionic detergent solutions; C_8E_4 (pink), NG (green), OGNG (purple) and DDM (orange). Membrane protein complexes from NG, OGNG and DDM possessed CCS values substantially larger than those calculated from crystal structures. **c,** Complete removal of C_8E_4 at low collision voltages reveals CCS values consistent with those calculated from their respective crystal structures. **d,** Reported are measured masses, standard deviations, and empirical T_0 values used for direct CCS calculation of membrane proteins studied.

a

Phospholipid Name	Abbreviation	Average Molecular Weight	Phospholipid Head Group
1,2-dinervonoyl-*sn*-glycero-3-phosphocholine (24:1 Cis)	DNPC	954.4	
1,2-dierucoyl-*sn*-glycero-3-phosphocholine (22:1 Cis)	DEPC	898.3	
1,2-dieicosenoyl-*sn*-glycero-3-phosphocholine (20:1 Cis)	DIPC	842.2	
1,2-dioleoyl-*sn*-glycero-3-phosphocholine (18:1 Cis)	DOPC	786.1	
1,2-dipalmitoleoyl-*sn*-glycero-3-phosphocholine (16:1 Cis)	DPPC	730.0	
1,2-dimyristoleoyl-*sn*-glycero-3-phosphocholine (14:1 Cis)	DMPC	673.9	
1-palmitoyl-2-oleoyl-*sn*-glycero-3-phosphocholine (16:0-18:1)	PC	760.1	
1-palmitoyl-2-oleoyl-*sn*-glycero-3-phospho-L-serine (16:0-18:1)	PS	784.0	
L-α-phosphatidylglycerol (*E. coli*)	PG	761.1	
1-palmitoyl-2-oleoyl-*sn*-glycero-3-phosphate (16:0-18:1)	PA	696.9	
L-α-phosphatidylethanolamine (*E. coli*)	PE	719.3	
1,2-dioleoyl-*sn*-glycero-3-phospho-(1'-myo-inositol-3'-phosphate) (18:1)	PI	977.1	
Cardiolipin (*E. coli*)	CDL	1430.0	

b

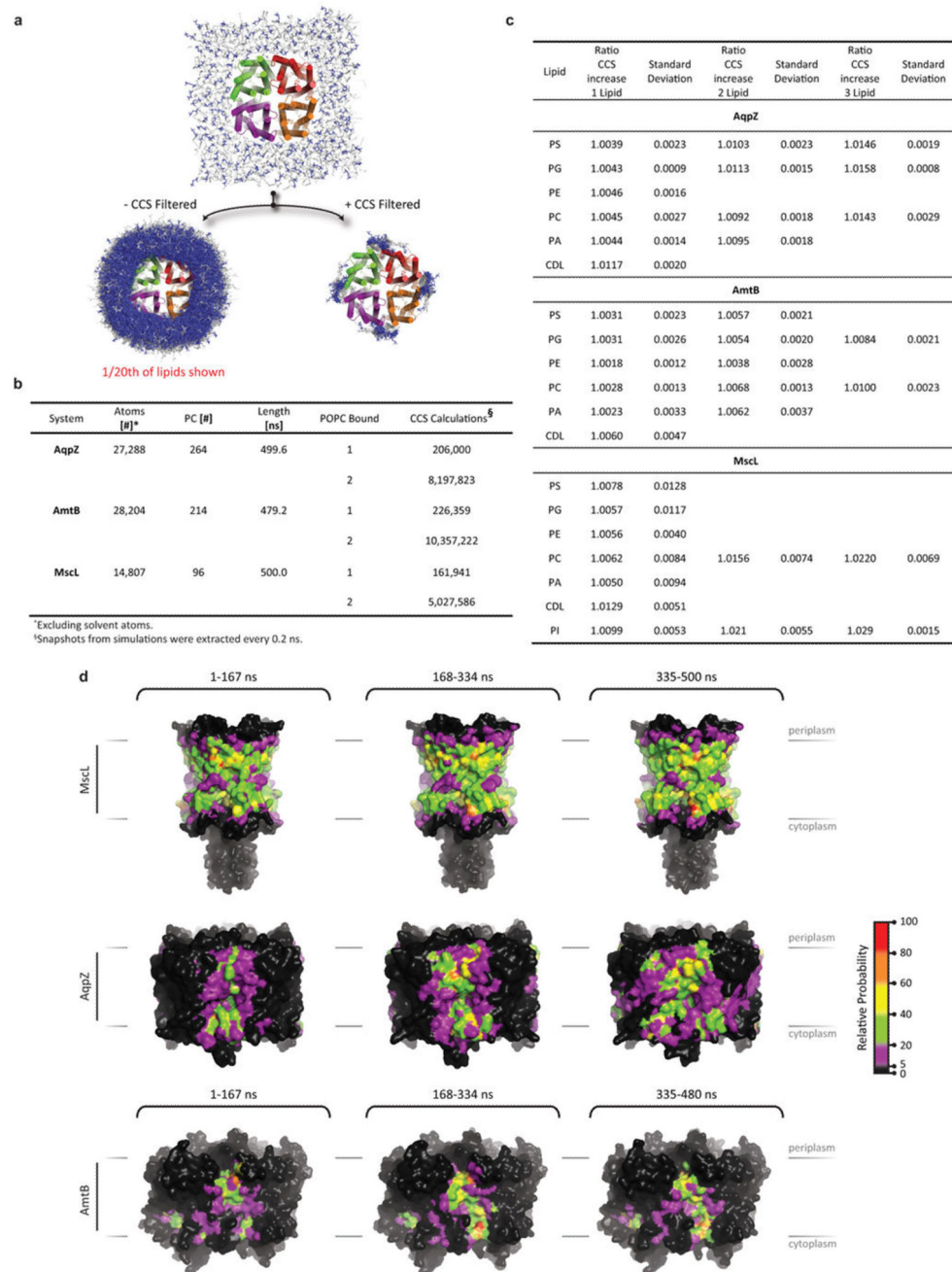| Protein	Phospholipid	Protein Oligomer (μM)	Phospholipid (μM)	Detergent (μM)	Ratio (P:L:D)	# Bound	Lipid mass addition (Da)
AqpZ	CDL	7	70	16300	1:10:2300	1	1378.5 ± 12.5
	PE	7	348	-	1:50:2300	1	718.2 ± 18.5
	PG	9	87	-	1:10:1757	3	767.6 ± 11.1
	PS	9	383	-	1:40:1757	3	785.5 ± 25.6
	PC	7	132	-	1:18:2300	3	762.3 ± 14.0
	PA	7	449	-	1:61:2300	2	658.2 ± 8.0
AmtB	CDL	3	140	16300	1:45:5197	1	1417.9 ± 68.1
	PE	2	70	-	1:44:10395	2	688.7 ± 29.1
	PG	4	99	-	1:28:4559	4	756.9 ± 20.8
	PS	4	92	-	1:26:4559	3	759.9 ± 22.9
	PC	4	95	-	1:27:4559	3	756.5 ± 20.9
	PA	2	69	-	1:44:10395	3	664.5 ± 14.0
AmtB[N72A/N79A]	PG	6	131	-	1:21:2558	3	763.1 ± 21.3
MscL	CDL	17	175	8157	1:10:480	1	1430.0 ± 41.7
	PE	17	70	-	1:4:480	1	705.5 ± 25.8
	PG	17	131	-	1:8:480	2	778.4 ± 39.4
	PS	17	128	-	1:7:480	2	794.8 ± 22.0
	PC	17	132	-	1:7:480	3	776.4 ± 29.7
	PA	17	143	-	1:8:480	1	672.7 ± 36.5
	PI	17	52	-	1:6:480	4	957.3 ± 13.8
	DNPC	24	79	-	1:3:350	2	967.5 ± 29.7
	DEPC	24	56	-	1:2:350	2	913.6 ± 13.9
	DIPC	24	89	-	1:4:350	2	830.2 ± 52.9
	DOPC	24	95	-	1:4:350	2	793.7 ± 22.2
	DPPC	24	137	-	1:6:350	2	752.9 ± 52.2
	DMPC	24	74	-	1:3:350	2	695.6 ± 54.9

Extended Data Figure 2. Phospholipid abbreviations and optimization of phospholipid binding experiments

a, Phospholipid abbreviations and headgroup structures. **b,** Protein to phospholipid to detergent ratios (P:L:D) for each membrane protein, number of resolvable phospholipids bound with their masses. Conditions were optimized empirically to maintain nanospray, sufficient mass spectral quality, and phospholipid binding. Masses for one lipid bound to the protein complex were measured using MassLynx V4.1 software (Waters).
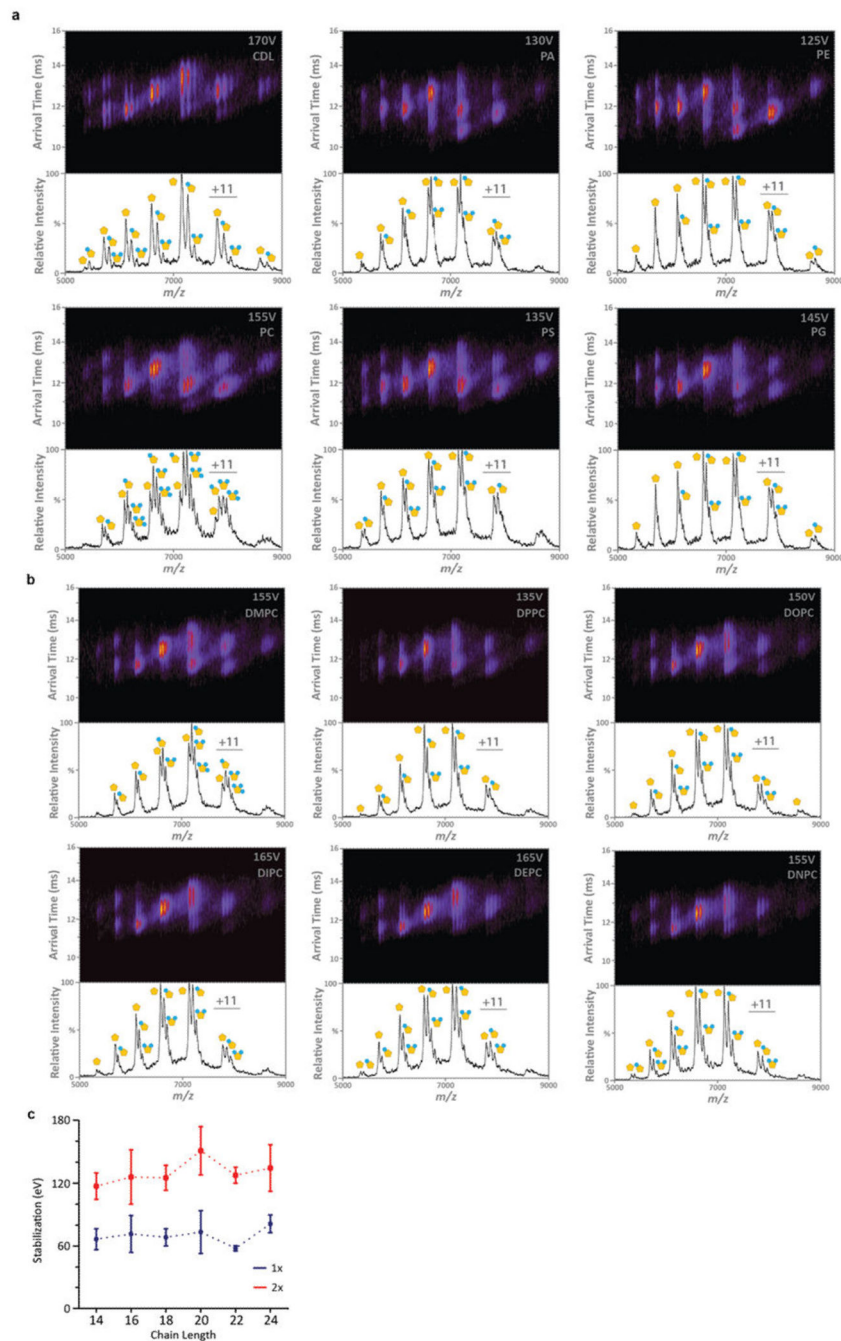
Extended Data Figure 3. Phospholipid binding to MscL reveals an insignificant impact on protein gas-phase stabilization independent of lipid alkyl chain length

a, Representative mass and ion mobility spectra of MscL bound to various phospholipids species (inset top right). **b,** Representative mass and ion mobility spectra of MscL bound to phospholipids of varying alkyl chain length. **c,** Cumulative stabilization of MscL is seen for one (blue) to two (red) bound lipid molecules. Reported are the mean ± SEM ($N = 3$).

a

- CCS Filtered   + CCS Filtered

1/20th of lipids shown

b

System	Atoms [#]*	PC [#]	Length [ns]	POPC Bound	CCS Calculations§
AqpZ	27,288	264	499.6	1	206,000
				2	8,197,823
AmtB	28,204	214	479.2	1	226,359
				2	10,357,222
MscL	14,807	96	500.0	1	161,941
				2	5,027,586

*Excluding solvent atoms.
§Snapshots from simulations were extracted every 0.2 ns.

c

Lipid	Ratio CCS increase 1 Lipid	Standard Deviation	Ratio CCS increase 2 Lipid	Standard Deviation	Ratio CCS increase 3 Lipid	Standard Deviation
			AqpZ			
PS	1.0039	0.0023	1.0103	0.0023	1.0146	0.0019
PG	1.0043	0.0009	1.0113	0.0015	1.0158	0.0008
PE	1.0046	0.0016				
PC	1.0045	0.0027	1.0092	0.0018	1.0143	0.0029
PA	1.0044	0.0014	1.0095	0.0018		
CDL	1.0117	0.0020				
			AmtB			
PS	1.0031	0.0023	1.0057	0.0021		
PG	1.0031	0.0026	1.0054	0.0020	1.0084	0.0021
PE	1.0018	0.0012	1.0038	0.0028		
PC	1.0028	0.0013	1.0068	0.0013	1.0100	0.0023
PA	1.0023	0.0033	1.0062	0.0037		
CDL	1.0060	0.0047				
			MscL			
PS	1.0078	0.0128				
PG	1.0057	0.0117				
PE	1.0056	0.0040				
PC	1.0062	0.0084	1.0156	0.0074	1.0220	0.0069
PA	1.0050	0.0094				
CDL	1.0129	0.0051				
PI	1.0099	0.0053	1.021	0.0055	1.029	0.0015

d

Extended Data Figure 4. Summary of statistics for molecular dynamics (MD) simulations followed by CCS filtering

a, Representative filtering procedure of AqpZ in a PC bilayer from the MD (top). For each frame, lipids are extracted within 6 Å of the protein (bottom left) then filtered by the experimental CCS of AqpZ bound to a single PC molecule (bottom right), see Methods. **b,** Summary of statistics. **c,** Ratios of phospholipid bound to *apo* CCS values for membrane protein complexes. Reported are the mean and standard deviation ($N = 3$). **d,** MD filtered by

CCS resulted in similar patches of PC molecules across different time points within the simulation indicating the systems were equilibrated.
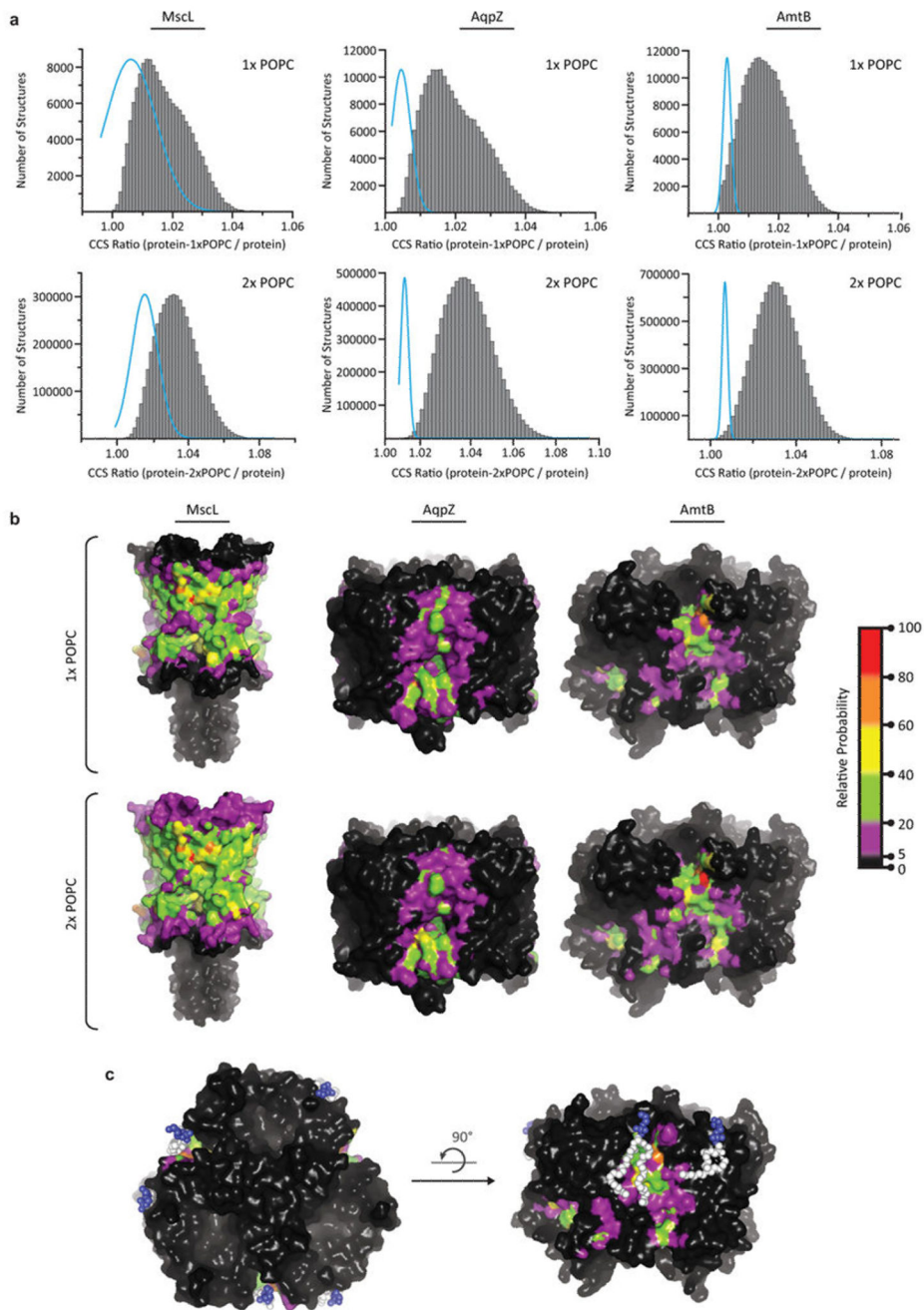
Extended Data Figure 5. MD simulations filtered by CCS reveals probable one (1x) and two (2x) phospholipid binding sites

a, For each candidate structure, protein and 1x or 2x PC molecule(s), the ratio of their calculated CCS values was determined (CCS Ratio). This procedure generated a large number of candidate structures (grey bars) that were filtered using our CCS measurements (cyan line). The structures in grey that intercept this curve are essentially the ones selected

as our most probable ensemble. **b,** The intersection between the simulated lipid complexes and the experimental data is then projected onto the surface of the protein to identify the most probable binding sites. Probable lipid locations for MscL resembled an annular belt, with no specific patches of lipids likely stemming from the relatively cylindrical geometry of this complex. By contrast for AqpZ and AmtB the most probable location of the lipid molecules were localized to the interfacial regions between protein subunits, as well as other probable locations on individual monomers. **c,** X-ray derived PG (blue spheres with white tails) located at the subunit interfaces agrees with the predicted PC binding site.
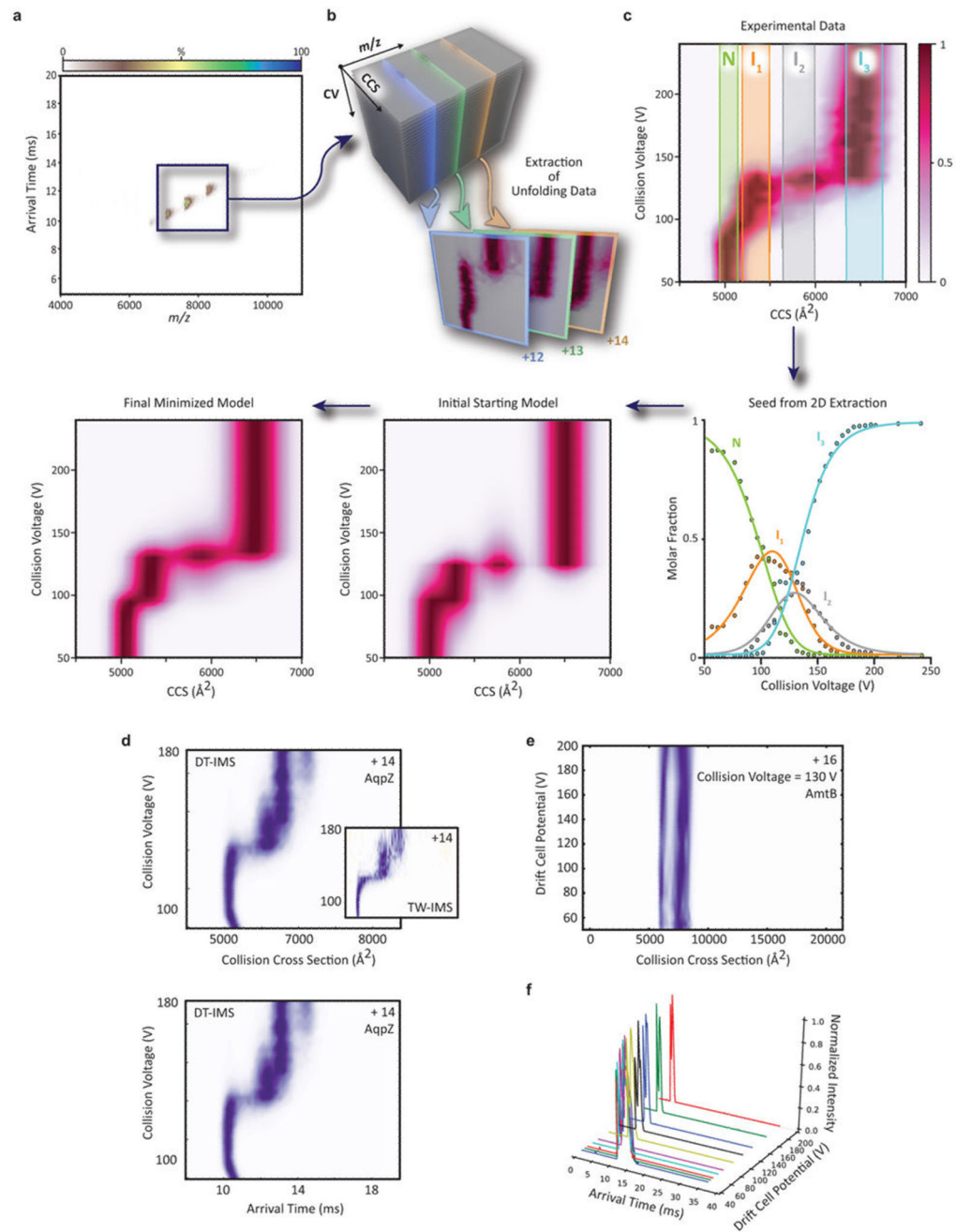
Extended Data Figure 6. Modeling and quantification of gas-phase unfolding pathways
a, Representative ion mobility mass spectra are collected over a range of collision voltages.
b, Ion arrival time is converted to CCS before generating unfolding plots. **c,** Model fitting
process from 2D to 3D data (See Methods). **d,** Both a Synapt2 modified with a linear drift
cell (DT-IMS) and the commercially available travelling wave SynaptG2 (TW-IMS)
produce qualitatively similar unfolding data. **e,** A contour plot representing the variance of
CCS of two gas-phase unfolding species as a function of ion mobility drift cell potential. **f,**
Stacked plots of arrival time distributions for two gas-phase unfolding species as a function

of drift cell potential. The lifetime of unfolding protein complexes in the drift tube ranges from 4 to 15 ms depending on the drift cell potential. No additional unfolding post activation occurs implying that the unfolding mechanism is not consistent with an irreversible unfolding model. Such a mechanism would predict time dependence on the population of unfolded species. By contrast the unfolding mechanism is well described by the reversible unfolding mechanism (see Methods).
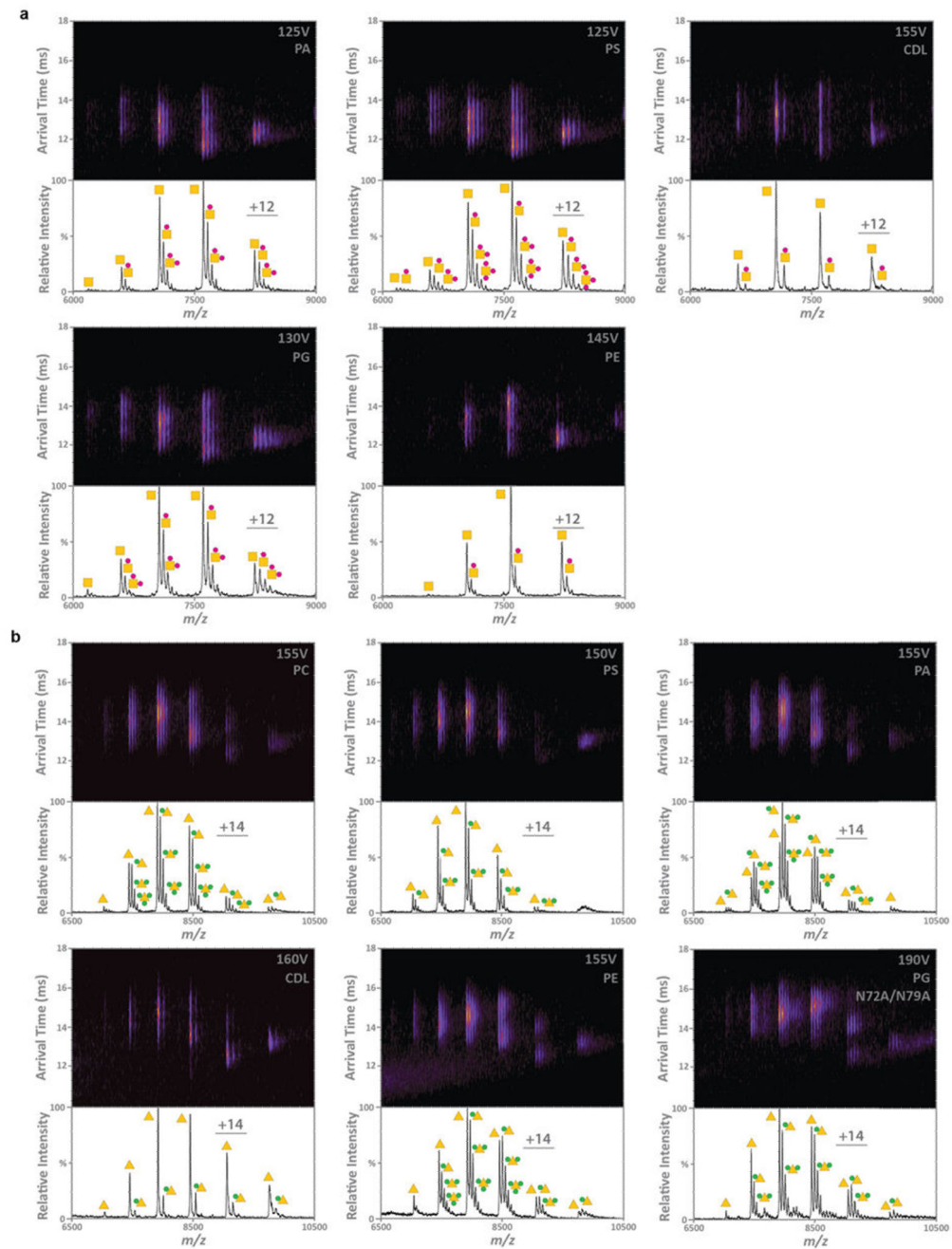
Extended Data Figure 7. AqpZ, AmtB and AmtB^N72A/N79A bound to various phospholipid species

a, Representative mass and ion mobility spectra of AqpZ bound to phospholipids. **b,** Representative mass and ion mobility spectra of AmtB bound to phospholipids and AmtB[N72A/N79A] bound to PG.

Lipid Extract	mol %		
	PE	PG	CDL
BKT22-YC	71.7	21.7	6.6
BKT22	74.2	25.8	-
EPL	72.9	18.0	9.1

Total Polar Lipid Extract	AqpZ	k_{wat} (s^{-1})	Standard Error
EPL	+	92.6	3.7
BKT22	+	35.6	5.6
BKT22-YC	+	82.9	5.1
EPL	-	1.2	0.023
BKT22	-	0.4	0.005
BKT22-YC	-	0.5	0.011
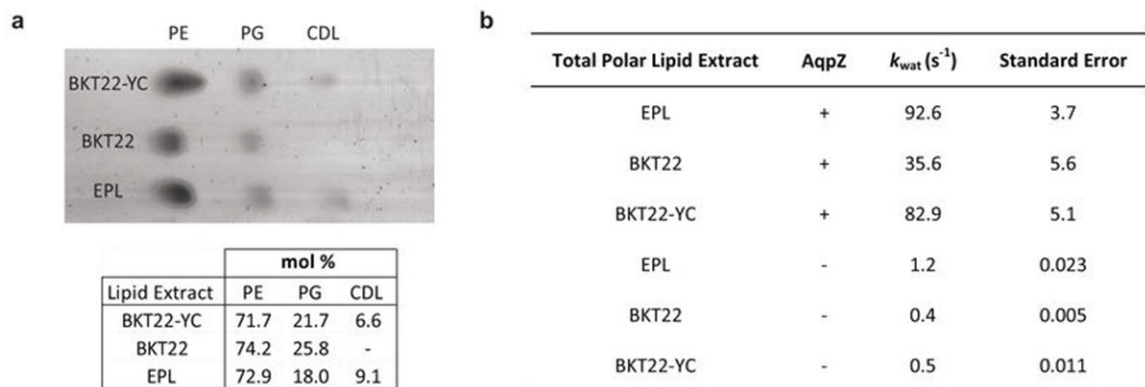
Extended Data Figure 8. Summary of water permeability assays and analysis of lipid extracts
a, HPTLC analysis of total polar lipid extract from wild-type *E. coli* (EPL), cardiolipin-deficient strain (BKT22), or BKT22 cells expressing ClsC and YmdB (BKT22-YC) to restore cardiolipin. Lipids were quantified by densiotometry. **b,** Reported are the rate constants (k_{wat}) and standard error of replicates ($N = 5$) for empty liposomes (−) and AqpZ proteoliposomes (+) reconstituted in differing *E. coli* lipid compositions.
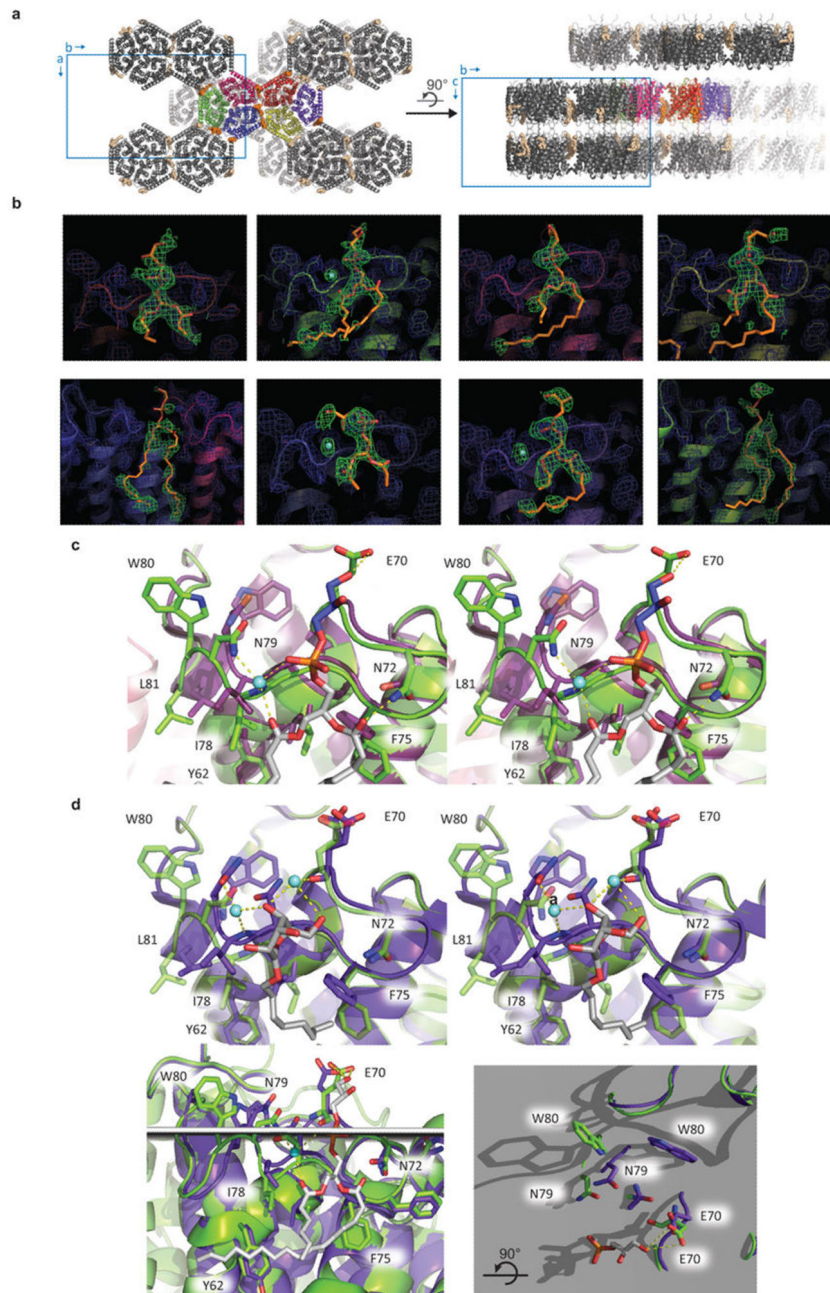
Extended Data Figure 9. Structural analysis of AmtB bound to PG
a, Crystal packing with Six AmtB (multicolored) and eight PG (orange) molecules located in the asymmetric unit cell and symmetry related molecules shown in grey and light orange, respectively. **b,** F_o-F_c and $2F_o$-F_c electron density maps after refinement without lipid and near-lipid water molecule (if present) contoured at 2.0 and 1.0 sigma, respectively. **c,** Comparison of AmtB bound to PG (green chain, this work) aligned with the AmtB structure (maroon chain, pdb 1U7G). **d,** Structure overlay of AmtB-GlnK complex bound to octylglucoside (purple chain, pdb 2NS1) aligned with AmtB bound to PG reveals a distinct

conformational change. The lipid-water interface (grey plane) was determined from coordinates of phosphate atoms from bound PG.

Extended Data Table 1

Summary of X-ray data collection and refinement statistics.

	AmtB bound to PG
Data collection	
Space group	$C222_1$
Cell dimensions	
a, b, c (Å)	116.2, 201.2, 232.5
α, β, γ (°)	90, 90, 90
Resolution (Å)	40-2.3 (2.4-2.3)*
R_{merge} (%)	12.4 (120.4)
$I / \sigma I$	13.7 (2.5)
Completeness (%)	99.9 (99.5)
Redundancy	11.0 (6.9)
Refinement	
Resolution (Å)	38.7-2.3 (2.36-2.3)
No. reflections	119,766
R_{work} / R_{free}	20.2 / 23.45[§]
No. atoms	
Protein	15,856
Ligand/ion	293
Water	111
B-factors	
Protein	45.3
Ligand/ion	64.7
Water	29.5
R.m.s. deviations	
Bond lengths (Å)	0.016
Bond angles (°)	1.71

[a]Values in parentheses are for highest-resolution shell.

[b]R_{free} calculated using 5% of the data.

Supplementary Material

Refer to Web version on PubMed Central for supplementary material.

Acknowledgements

References

1. Singer SJ, Nicolson GL. The fluid mosaic model of the structure of cell membranes. Science. 1972; 175:720–731. [PubMed: 4333397]

2. Cantor RS. The influence of membrane lateral pressures on simple geometric models of protein conformational equilibria. Chem Phys Lipids. 1999; 101:45–56. [PubMed: 10810924]

3. Hunte C, Richers S. Lipids and membrane protein structures. Curr Opin Struct Biol. 2008; 18:406–411. doi:10.1016/j.sbi.2008.03.008. [PubMed: 18495472]

4. Lee AG. Biological membranes: the importance of molecular detail. Trends Biochem Sci. 2011; 36:493–500. doi:10.1016/j.tibs.2011.06.007. [PubMed: 21855348]

5. Sanders CR, Mittendorf KF. Tolerance to changes in membrane lipid composition as a selected trait of membrane proteins. Biochemistry. 2011; 50:7858–7867. doi:10.1021/bi2011527. [PubMed: 21848311]

6. Contreras FX, Ernst AM, Wieland F, Brugger B. Specificity of intramembrane protein-lipid interactions. Cold Spring Harb Perspect Biol. 2011; 3 doi:10.1101/cshperspect.a004705.

7. Whitelegge JP. Integral membrane proteins and bilayer proteomics. Anal Chem. 2013; 85:2558–2568. doi:10.1021/ac303064a. [PubMed: 23301778]

8. Long SB, Tao X, Campbell EB, MacKinnon R. Atomic structure of a voltage-dependent K+ channel in a lipid membrane-like environment. Nature. 2007; 450:376–382. doi:10.1038/nature06265. [PubMed: 18004376]

9. Zhong D, Blount P. Phosphatidylinositol Is Crucial for the Mechanosensitivity of Mycobacterium tuberculosis MscL. Biochemistry. 2013; 52:5415–5420. doi:10.1021/bi400790j. [PubMed: 23875651]

10. Chang G, Spencer RH, Lee AT, Barclay MT, Rees DC. Structure of the MscL homolog from Mycobacterium tuberculosis: a gated mechanosensitive ion channel. Science. 1998; 282:2220–2226. [PubMed: 9856938]

11. Haswell ES, Phillips R, Rees DC. Mechanosensitive channels: what can they do and how do they do it? Structure. 2011; 19:1356–1369. doi:10.1016/j.str.2011.09.005. [PubMed: 22000509]

12. Savage DF, Egea PF, Robles-Colmenares Y, O'Connell JD 3rd, Stroud RM. Architecture and selectivity in aquaporins: 2.5 a X-ray structure of aquaporin Z. PLoS Biol. 2003; 1:E72. doi:10.1371/journal.pbio.0000072. [PubMed: 14691544]

13. Gonen T, et al. Lipid-protein interactions in double-layered two-dimensional AQP0 crystals. Nature. 2005; 438:633–638. doi:10.1038/nature04321. [PubMed: 16319884]

14. Khademi S, et al. Mechanism of ammonia transport by Amt/MEP/Rh: structure of AmtB at 1.35 A. Science. 2004; 305:1587–1594. doi:10.1126/science.1101952. [PubMed: 15361618]

15. Barrera NP, Di Bartolo N, Booth PJ, Robinson CV. Micelles protect membrane complexes from solution to vacuum. Science. 2008; 321:243–246. doi:10.1126/science.1159292. [PubMed: 18556516]

16. Laganowsky A, Reading E, Hopper JT, Robinson CV. Mass spectrometry of intact membrane protein complexes. Nat Protoc. 2013; 8:639–651. doi:10.1038/nprot.2013.024. [PubMed: 23471109]

17. Ruotolo BT, et al. Evidence for macromolecular protein rings in the absence of bulk water. Science. 2005; 310:1658–1661. doi:10.1126/science.1120177. [PubMed: 16293722]

18. Baldwin AJ, et al. The polydispersity of alphaB-crystallin is rationalized by an interconverting polyhedral architecture. Structure. 2011; 19:1855–1863. doi:10.1016/j.str.2011.09.015. [PubMed: 22153508]

19. Hyung SJ, Robinson CV, Ruotolo BT. Gas-phase unfolding and disassembly reveals stability differences in ligand-bound multiprotein complexes. Chem Biol. 2009; 16:382–390. doi:10.1016/j.chembiol.2009.02.008. [PubMed: 19389624]

20. Pace CN. Determination and analysis of urea and guanidine hydrochloride denaturation curves. Methods Enzymol. 1986; 131:266–280. [PubMed: 3773761]

21. Hong, H.; Joh, NH.; Bowie, JU.; Tamm, LK. Methods Enzymol. Holt, Jo M.; Johnson, Michael L.; Gary, K. Ackers, editors. Vol. Vol. Volume 455. Academic Press; 2009. p. 213-236.

22. Powl AM, East JM, Lee AG. Lipid-protein interactions studied by introduction of a tryptophan residue: the mechanosensitive channel MscL. Biochemistry. 2003; 42:14306–14317. doi:10.1021/bi034995k. [PubMed: 14640699]

23. Borgnia MJ, Kozono D, Calamita G, Maloney PC, Agre P. Functional reconstitution and characterization of AqpZ, the E. coli water channel protein. J Mol Biol. 1999; 291:1169–1179. doi:10.1006/jmbi.1999.3032. [PubMed: 10518952]

24. Tan BK, et al. Discovery of a cardiolipin synthase utilizing phosphatidylethanolamine and phosphatidylglycerol as substrates. Proc Natl Acad Sci U S A. 2012; 109:16504–16509. doi:10.1073/pnas.1212797109. [PubMed: 22988102]

25. Yau WM, Wimley WC, Gawrisch K, White SH. The preference of tryptophan for membrane interfaces. Biochemistry. 1998; 37:14713–14718. doi:10.1021/bi980809c. [PubMed: 9778346]

26. Iscla I, Blount P. Sensing and responding to membrane tension: the bacterial MscL channel as a model system. Biophys J. 2012; 103:169–174. doi:10.1016/j.bpj.2012.06.021. [PubMed: 22853893]

27. Hite RK, Li Z, Walz T. Principles of membrane protein interactions with annular lipids deduced from aquaporin-0 2D crystals. EMBO J. 2010; 29:1652–1658. doi:10.1038/emboj.2010.68. [PubMed: 20389283]

28. Romantsov T, Battle AR, Hendel JL, Martinac B, Wood JM. Protein localization in Escherichia coli cells: comparison of the cytoplasmic membrane proteins ProP, LacY, ProW, AqpZ, MscS, and MscL. J Bacteriol. 2010; 192:912–924. doi:10.1128/jb.00967-09. [PubMed: 20008071]

29. Blakey D, et al. Purification of the Escherichia coli ammonium transporter AmtB reveals a trimeric stoichiometry. Biochem J. 2002; 364:527–535. doi:10.1042/bj20011761. [PubMed: 12023896]

30. Engelman DM. Membranes are more mosaic than fluid. Nature. 2005; 438:578–580. doi:10.1038/nature04394. [PubMed: 16319876]

31. Gandhi CS, Walton TA, Rees DC. OCAM: a new tool for studying the oligomeric diversity of MscL channels. Protein Sci. 2011; 20:313–326. doi:10.1002/pro.562. [PubMed: 21280123]

32. Hilf RJ, Dutzler R. X-ray structure of a prokaryotic pentameric ligand-gated ion channel. Nature. 2008; 452:375–379. doi:10.1038/nature06717. [PubMed: 18322461]

33. Lee D, et al. Gene doctoring: a method for recombineering in laboratory and pathogenic Escherichia coli strains. BMC Microbiology. 2009; 9:252. [PubMed: 20003185]

34. Drew D, Lerch M, Kunji E, Slotboom DJ, de Gier JW. Optimization of membrane protein overexpression and purification using GFP fusions. Nat Methods. 2006; 3:303–313. doi:10.1038/nmeth0406-303. [PubMed: 16554836]

35. Newby ZE, et al. A general protocol for the crystallization of membrane proteins for X-ray structural investigation. Nat Protoc. 2009; 4:619–637. doi:10.1038/nprot.2009.27. [PubMed: 19360018]

36. Laganowsky A, et al. Crystal structures of truncated alphaA and alphaB crystallins reveal structural mechanisms of polydispersity important for eye lens function. Protein Sci. 2010; 19:1031–1043. doi:10.1002/pro.380. [PubMed: 20440841]

37. Laganowsky A, et al. Atomic View of a Toxic Amyloid Small Oligomer. Science. 2012; 335:1228–1231. doi:10.1126/science.1213151. [PubMed: 22403391]

38. Gasteiger E,HC, Gattiker A, Duvaud S, Wilkins MR, Appel RD, Bairoch A. Protein Identification and Analysis Tools on the ExPASy Server. 2005:571–607.

39. Savage DF, O'Connell JD 3rd, Miercke LJ, Finer-Moore J, Stroud RM. Structural context shapes the aquaporin selectivity filter. Proc Natl Acad Sci U S A. 2010; 107:17164–17169. doi:10.1073/pnas.1009864107. [PubMed: 20855585]

40. Sobott F, Hernandez H, McCammon MG, Tito MA, Robinson CV. A tandem mass spectrometer for improved transmission and analysis of large macromolecular assemblies. Anal Chem. 2002; 74:1402–1407. [PubMed: 11922310]

41. Bush MF, et al. Collision cross sections of proteins and their complexes: a calibration framework and database for gas-phase structural biology. Anal Chem. 2010; 82:9557–9565. doi:10.1021/ac1022953. [PubMed: 20979392]

42. Mason EA, Schamp HW. MOBILITY OF GASEOUS IONS IN WEAK ELECTRIC FIELDS. Annals of Physics. 1958; 4:233–270. doi:10.1016/0003-4916(58)90049-6.

43. Shvartsburg AA, Jarrold MF. An exact hard-spheres scattering model for the mobilities of polyatomic ions. Chemical Physics Letters. 1996; 261:86–91. doi:10.1016/0009-2614(96)00941-4.

44. Mesleh MF, Hunter JM, Shvartsburg AA, Schatz GC, Jarrold MF. Structural Information from Ion Mobility Measurements: Effects of the Long-Range Potential. J Phys Chem. 1996; 100:16082–16086. doi:10.1021/jp961623v.

45. Benesch JLP, Ruotolo BT. Mass spectrometry: come of age for structural and dynamical biology. Curr Opin Struc Biol. 2011; 21:641–649. doi:10.1016/j.sbi.2011.08.002.

46. Hall Z, Politis A, Robinson CV. Structural Modeling of Heteromeric Protein Complexes from Disassembly Pathways and Ion Mobility-Mass Spectrometry. Structure. 2012; 20:1596–1609. doi: 10.1016/j.str.2012.07.001. [PubMed: 22841294]

47. Ruotolo BT, Benesch JL, Sandercock AM, Hyung SJ, Robinson CV. Ion mobility-mass spectrometry analysis of large protein complexes. Nat Protoc. 2008; 3:1139–1152. doi:10.1038/ nprot.2008.78. [PubMed: 18600219]

48. Stengel F, et al. Dissecting heterogeneous molecular chaperone complexes using a mass spectrum deconvolution approach. Chem Biol. 2012; 19:599–607. doi:10.1016/j.chembiol.2012.04.007. [PubMed: 22633411]

49. Hunter JD. Matplotlib: A 2D graphics environment. Computing In Science & Engineering. 2007; 9:90–95.

50. Jones, E.; Oliphant, T.; Peterson, P., et al. Scipy: Open source scientific tools for Python. 2001. http://www.scipy.org

51. Izzo D, Ruci ski M, Biscani F. The Generalized Island Model. Parallel Architectures and Bioinspired Algorithms. 2012:151–169.

52. Izzo, D. PYGMO AND PYKEP: OPEN SOURCE TOOLS FOR MASSIVELY PARALLEL OPTIMIZATION IN ASTRODYNAMICS (THE CASE OF INTERPLANETARY TRAJECTORY OPTIMIZATION). Proceedings of the Fifth International Conference on Astrodynamics Tools and Techniques, ICATT; 2012.

53. Berendsen HJC, van der Spoel D, van Drunen R. GROMACS: A message-passing parallel molecular dynamics implementation. Computer Physics Communications. 1995; 91:43–56. http:// dx.doi.org/10.1016/0010-4655(95)00042-E.

54. Jorgensen WL, Maxwell DS, Tirado-Rives J. Development and Testing of the OPLS All-Atom Force Field on Conformational Energetics and Properties of Organic Liquids. Journal of the American Chemical Society. 1996; 118:11225–11236. doi:10.1021/ja9621760.

55. Ulmschneider JP, Ulmschneider MB. Sampling efficiency in explicit and implicit membrane environments studied by peptide folding simulations. Proteins. 2009; 75:586–597. doi:10.1002/ prot.22270. [PubMed: 19003985]

56. Jorgensen WL, Chandrasekhar J, Madura JD, Impey RW, Klein ML. Comparison of simple potential functions for simulating liquid water. The Journal of Chemical Physics. 1983; 79:926–935. http://dx.doi.org/10.1063/1.445869.

57. Darden T, York D, Pedersen L. Particle mesh Ewald: An N log(N) method for Ewald sums in large systems. The Journal of Chemical Physics. 1993; 98:10089–10092. http://dx.doi.org/ 10.1063/1.464397.

58. Hess B, Bekker H, Berendsen HJC, Fraaije JGEM. LINCS: A linear constraint solver for molecular simulations. Journal of Computational Chemistry. 1997; 18:1463–1472. doi:10.1002/ (sici)1096-987x(199709)18:12<1463::aid-jcc4>3.0.co;2-h.

59. Bussi G, Donadio D, Parrinello M. Canonical sampling through velocity rescaling. The Journal of Chemical Physics. 2007; 126 http://dx.doi.org/10.1063/1.2408420.

60. Berendsen HJC, Postma JPM, van Gunsteren WF, DiNola A, Haak JR. Molecular dynamics with coupling to an external bath. The Journal of Chemical Physics. 1984; 81:3684–3690. http:// dx.doi.org/10.1063/1.448118.

61. Folch J, Lees M, Sloane Stanley GH. A simple method for the isolation and purification of total lipides from animal tissues. J Biol Chem. 1957; 226:497–509. [PubMed: 13428781]

62. Fine JB, Sprecher H. Unidimensional thin-layer chromatography of phospholipids on boric acid-impregnated plates. J Lipid Res. 1982; 23:660–663. [PubMed: 7097131]

63. Tan BK, et al. Discovery of a cardiolipin synthase utilizing phosphatidylethanolamine and phosphatidylglycerol as substrates. Proceedings of the National Academy of Sciences. 2012; 109:16504–16509. doi:10.1073/pnas.1212797109.

64. Schneider CA, Rasband WS, Eliceiri KW. NIH Image to ImageJ: 25 years of image analysis. Nat Meth. 2012; 9:671–675.

65. Kabsch W. XDS. Acta Crystallogr D Biol Crystallogr. 66:125–132. [PubMed: 20124692]

66. McCoy AJ, et al. Phaser crystallographic software. J Appl Crystallogr. 2007; 40:658–674. [PubMed: 19461840]

67. Padilla JE, Yeates TO. A statistic for local intensity differences: robustness to anisotropy and pseudo-centering and utility for detecting twinning. Acta Crystallogr D Biol Crystallogr. 2003; 59:1124–1130. [PubMed: 12832754]

68. Adams PD, et al. PHENIX: building new software for automated crystallographic structure determination. Acta Crystallogr D Biol Crystallogr. 2002; 58:1948–1954. [PubMed: 12393927]

69. Emsley P, Cowtan K. Coot: model-building tools for molecular graphics. Acta Crystallogr D Biol Crystallogr. 2004; 60:2126–2132. [PubMed: 15572765]

70. Murshudov GN, Vagin AA, Dodson EJ. Refinement of macromolecular structures by the maximum-likelihood method. Acta Crystallogr D Biol Crystallogr. 1997; 53:240–255. [PubMed: 15299926]

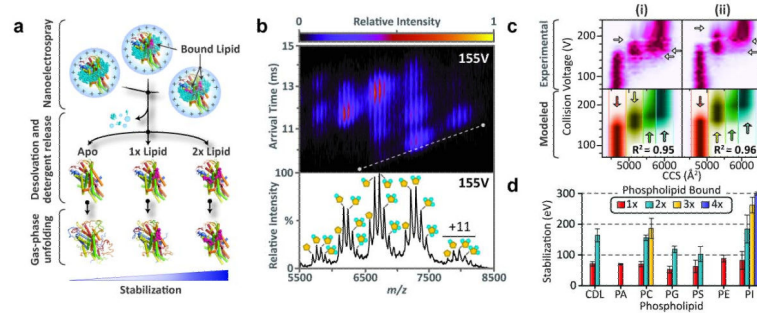71. Schrodinger, LLC. The PyMOL Molecular Graphics System. Version 1.3r12010.

Figure 1. The mechanosensitive channel of large conductance (MscL) resists unfolding in the presence of lipids

a, MscL in electrospray droplets, within a lipid-detergent micelle, undergoes desolvation and activation. **b,** Mass spectrum reveals multiple MscL phosphatidylinositol phosphate (PI) bound states. Ion mobility (top) of MscL(PI)$_{0-5}$ with a trend line for native state (dotted). **c,** Plot of collision voltage against CCS for +12 ions of *apo* (i) and MscL(PI)$_4$ (ii). Experimental and modeled unfolding plots with collision voltages at which transitions occur and CCS values (horizontal and vertical arrows respectively). R^2 values are provided. **d,** Stabilization calculated from parameters defined by fitting MscL (+12) with lipids. Reported are average and s.e.m. (*N=3*) in units of electron volts (eV).
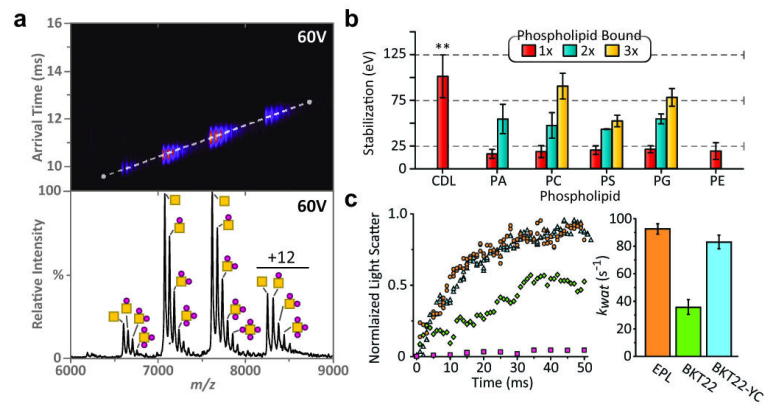
Figure 2. AqpZ is stabilized indiscriminately by lipids with the exception of cardiolipin, a lipid that stabilizes the channel significantly and modulates its function
a, Mass spectra reveal AqpZ(POPC)$_{0-5}$ resolved at 60 V with IM-MS arrival times in agreement with the CCS calculated from the crystal structure. **b,** Stabilization of AqpZ (+13) bound to lipids, calculated from unfolding parameters. One-way ANOVA ($N = 3$): **$P <$ 0.01. **c,** Water permeability assay for AqpZ reconstituted in total polar lipid extracts from *E. coli* (EPL) (orange), or a cardiolipin-deficient strain[24] (BKT22) (green), or BKT22 cells expressing ClsC and YmdB to restore cardiolipin (BKT22-YC) (cyan) are compared with empty EPL liposomes (pink) (Supplementary Figure 7). Rate constants of water transport (k_{wat}) and standard error of replicates ($N = 5$).
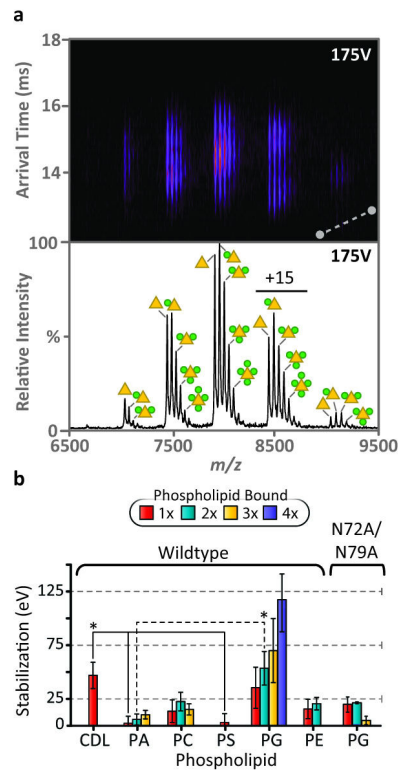
Figure 3. Lipid binding to AmtB results in a range of stabilizing effects

a, Ion mobility mass spectra of AmtB(PG)$_{0-4}$ molecules at 175V with IM-MS unfolding data as described in Fig. 1b. Arrival times for the various charge states reveal non-native, trimeric structures. **b,** Stabilization of AmtB (+15) bound to different lipids and AmtB[N72A/N79A] (+15) a mutant form designed to disrupt the specific PG-lipid binding site. Gas-phase unfolding reveals that AmtB is weakly stabilized by the majority of lipids but CDL and PG confer significant stabilization. AmtB[N72A/N79A] shows a reduction in stabilization by PG compared with the wild-type protein. Results are shown as in Fig. 2b with *$P < 0.05$.
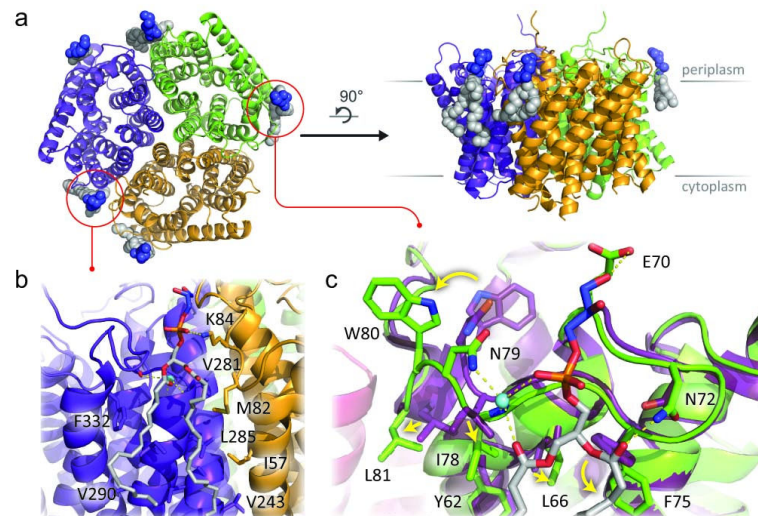
Figure 4. Crystal structure of AmtB bound to PG

a, AmtB, in cartoon representation, is viewed from the periplasm and perpendicular to the membrane plane. Resolved PG molecules (spheres) are oriented with headgroups on the periplasmic side, in the outer leaflet of the inner membrane. **b,** PG molecules at subunit interface are shown with residue labels and hydrophobic residues in contact with lipid tails (stick representation). Hydrogen bonds (dashed lines) are formed between phospho headgroup and K84, and a water bridge (aqua sphere). **c,** Conformational change of (yellow arrows) residues 70-81, induced by binding PG. Superposition of AmtB structure without lipid (PDB 1U7G, purple) bound to PG (green).